XXXVI International Workshop on High Energy Physics
Logunov IHEP of NRC “Kurchatov Institute”, Protvino, Russia, July 23 – 25, 2024

Collective effects in strong interaction processes: experimental highlights

V.A. Okorokov

MEPhI, Moscow, Russia

Outline

1. Introduction

2. Facilities and detectors

3. Some results for collectivity
   - Jets
   - Femtoscopic correlations
   - Bose–Einstein condensation

4. Closing remarks

Collectivity in strong interaction

The general and well-established picture of strong interaction reaction leads to the hypothesis that collective behavior and corresponding effects are deeply intrinsic properties of strong interaction driven by the dynamics of the collision process at all stages of its space-time evolution.

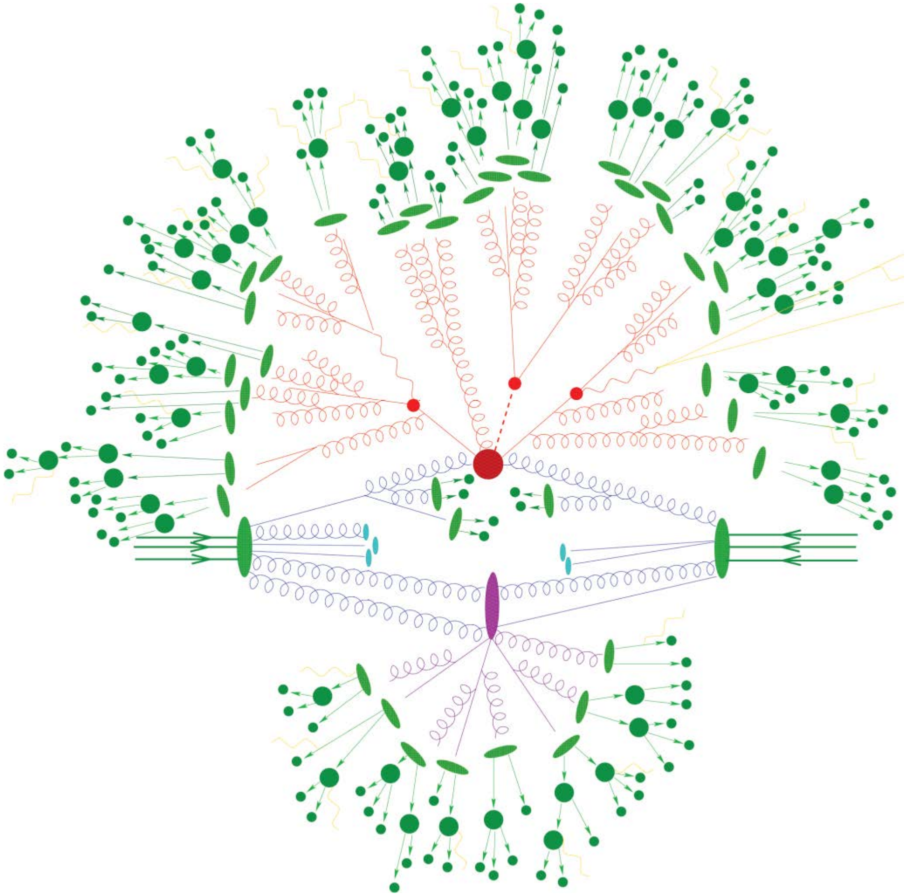

Fig. 1. Sketch of a hard hadron-hadron collision at a hadron collider experiment, such as the LHC. It depicts the hard interaction as the central, red blob. The initial and final state particles experience initial and finalstate radiation, in blue and red, respectively, leading to a proliferation of a large number of secondaries. The underlying event – in purple – has other partons scattering and producing further activity through multiple secondary emissions. All emerging partons will at some point arrive at low scales, and hadronize, before the primary hadrons produced there will decay further (in green) [1].

Importance of collective effects

Investigations of collective effects and collective modes of excitation of the hadronic (quark-gluon) matter provide unique information and are among the most promising and relevant for constructing a complete theory of strong interactions and studying of quantum multiparticle systems.

The study of collective and correlation characteristics of strong interaction makes it possible to draw conclusions regarding the space-time evolution of the interaction process and to establish a fundamental relationship between the geometry and dynamics of the creation of a final state.

Experimental base

During XXI century the main part of experimental and theoretical studies within strong interaction physics is based on the research works making at

– Relativistic Heavy Ion Collider (RHIC)

and the

– Large Hadron Collider (LHC).

Therefore the consideration below is focused on the results obtained at these facilities.

RHIC facility

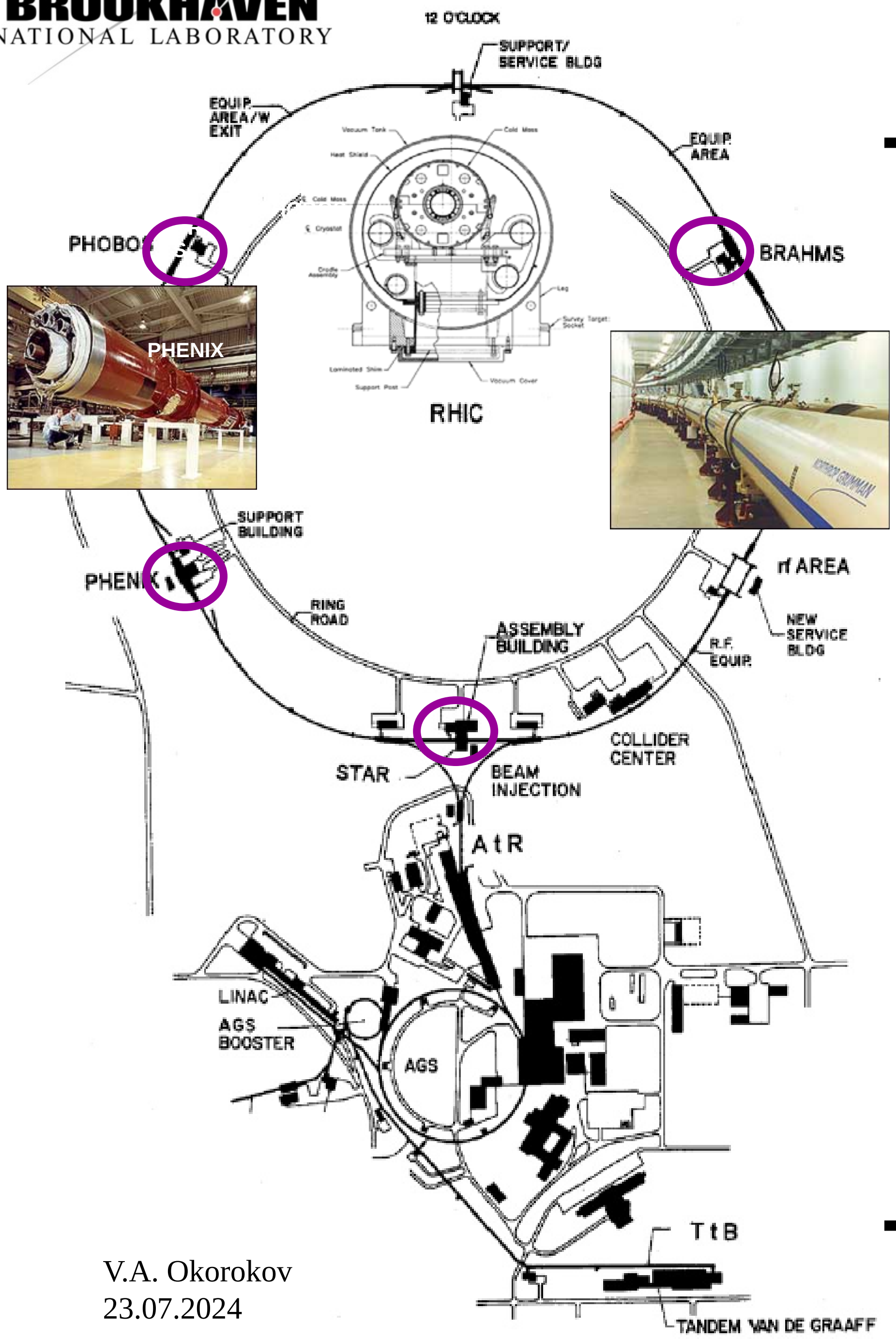

Relativistic Heavy Ion Collider

1. The complex was designed and was built for investigations in QCD field specially.

2. **23** successful physics runs since 2000 year. Run 24 is in the progress.

3. Experiments:
- large STAR continue to collect new data since 2000, large sPHENIX was commissioned in 2023;

- small BRAMS and PHOBOS were finished about 15 years ago, large PHENIX completed the data taking in 2016.

Fig. 2. Arrangement of detector along the RHIC ring [2].

RHIC: data collection

The data samples taken at RHIC since 2000 are shown in Table 1.

Table 1. Data samples from RHIC

Species	$\sqrt{s_{NN}}$, GeV
$p + p^{a}$	22.0^{b}, 62.4, 200, 410^{b}, 500, 510
p + Al	200
O + O	200^{b}
p^{a} + Au	200
d + Au	19.6, 39.0, 62.4, 200
^{3}He + Au	200
Al + Au	4.9^{c}, 200
Cu + Cu	22.4^{b}, 62.4, 200
Zr + Zr, Ru + Ru^{d}	200
Cu + Au	200
Au + Au	FXT^{c}: 3.0, 3.2, 3.5, 3.9, 4.5, 5.2, 6.2, 7.2, 7.7; 7.7, 9.2^{b}, 11.5, 14.6, 17.3, 19.6, 27.0, 39.0, 54.4^{b}, 55.8^{b}, 62.4, 130, 200
U + U	193

Note: [a]*with unpolarized ($\sqrt{s}$ = 62.4 GeV) and with longitudinal / transverse polarized beams;* [b]*run with small integral luminosity,* [c]*run in fixed target mode,* [d]*run with isobar beams ($A_{zr,Ru} = 96$, $Z_{Zr} = 40$, $Z_{Ru} = 44$)*

RHIC: detectors

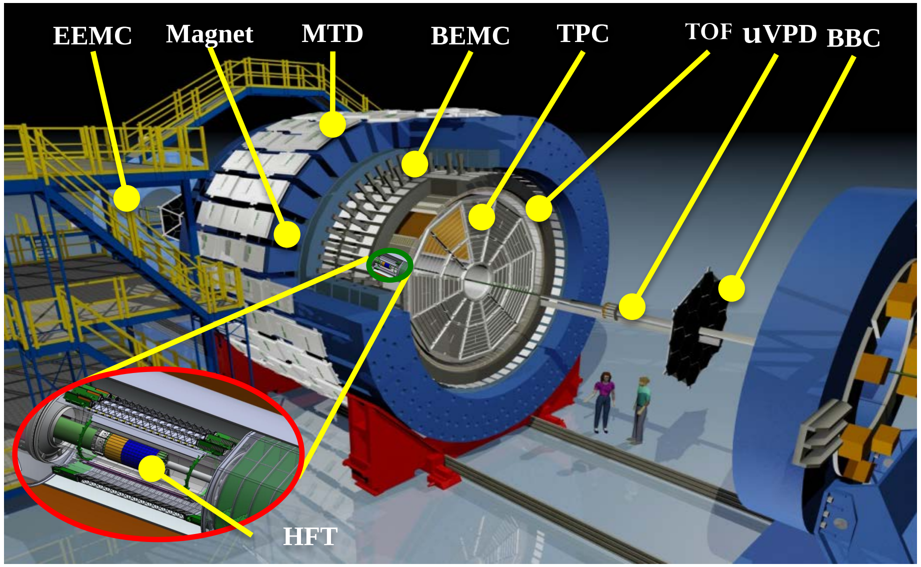

The sPHENIX and STAR detectors are characterized by good particle identification and uniform, large acceptance.

Both detectors are suitable rather good for study of various collective effects.

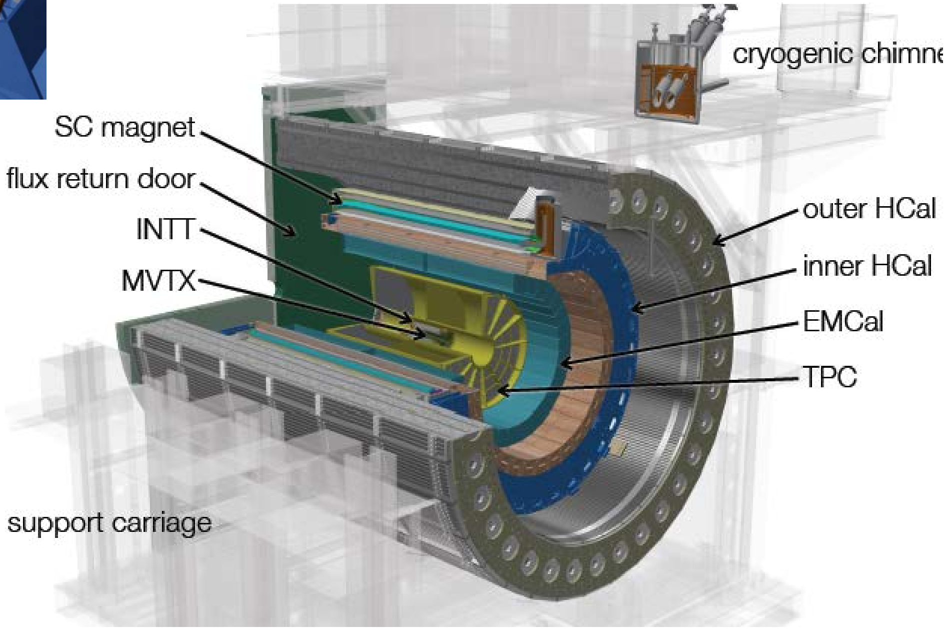

Fig. 3. General view of the STAR (left up) and sPHENIX (right bottom) detectors.

Study of collective effects at RHIC

The sPHENIX detector enables measurements of jet production and its substructure, open and hidden heavy flavor over an unprecedented kinematic range at RHIC.

The large acceptance of STAR makes it particularly well suited for study of wide set of collective effects in multiparticle production processes, for instance, correlations in soft sector of strong interaction and hadronic jets with large transverse momenta (p_T).

LHC facility

Large Hadron Collider

1. The complex was designed and was built for investigations in fundamental physics, in particular, in subfield of QCD.

2. **2** successful physics runs since 2009 year (1st 2009 – 2013, 2d 2015 – 2018). Run 3 (2022 – 2025) is in the progress.

3. Experiments:
- large ALICE, ATLAS, CMS and LHCb collect new data since 2009.

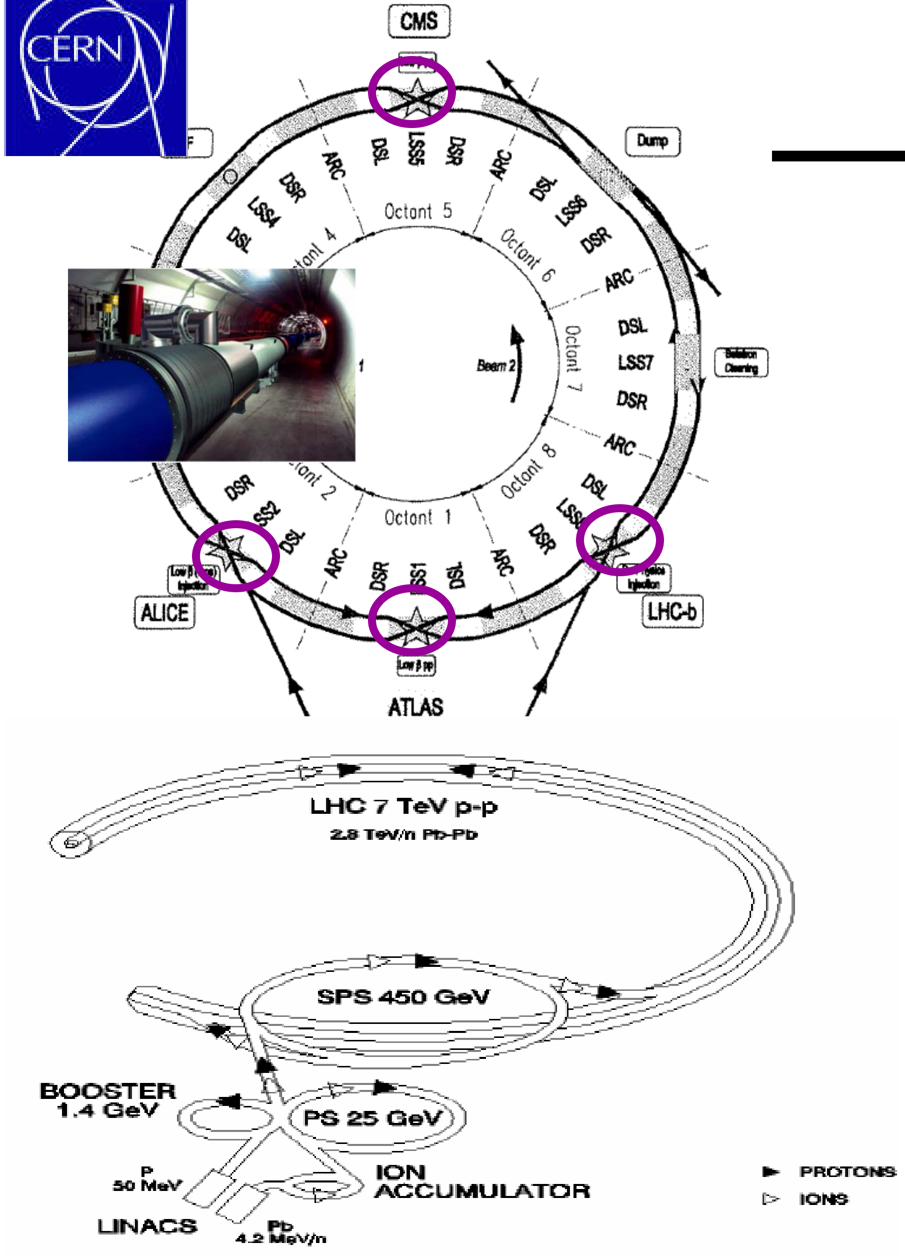

Fig. 4. Schematic layout of the LHC [3, 4] and the LHC injection complex [5].

LHC: large detectors (1)

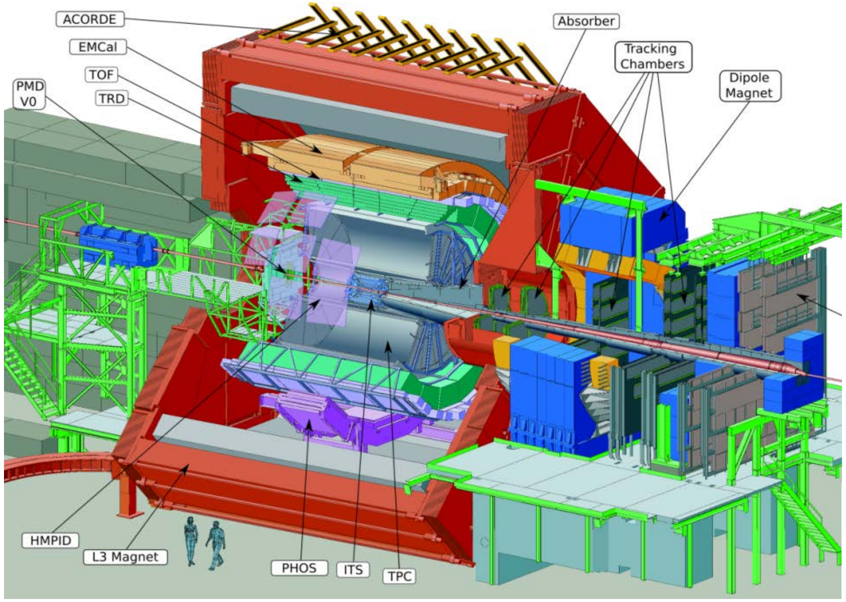

The ALICE and ATLAS detectors are characterized by good particle identification and (quasi)uniform, large acceptance.

Both detectors are suitable rather good for study of various collective effects.

Fig. 5. General view of the ALICE (left up) and ATLAS (right bottom) detectors.

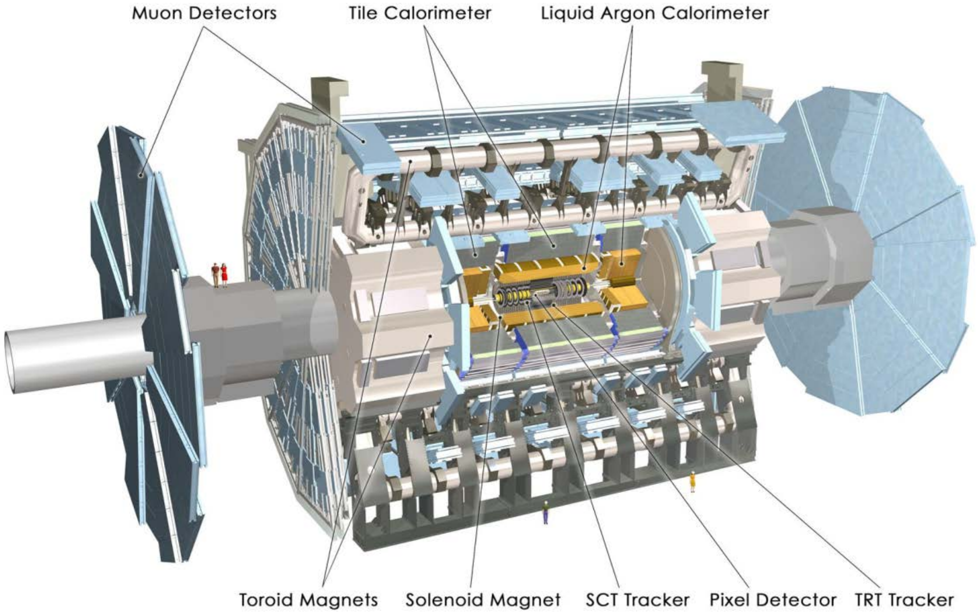

LHC: large detectors (2)

The CMS detectors is characterized by good particle identification and uniform, large acceptance. That detector is suitable rather good for study of various collective effects.

The feature of the LHCb is the excellent capability for reconstructing of heavy flavor particles (B-mesons).

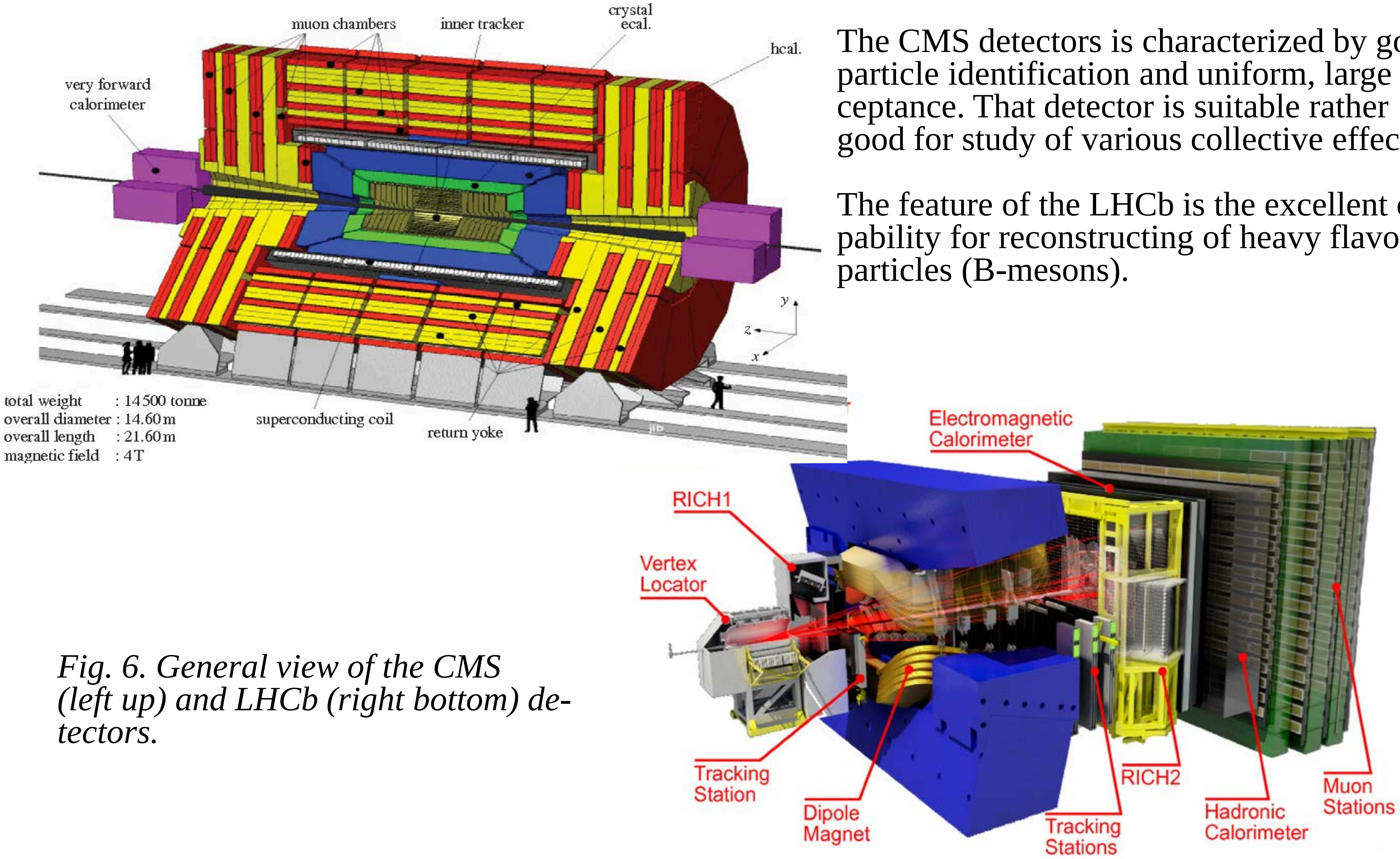

Fig. 6. General view of the CMS (left up) and LHCb (right bottom) detectors.

LHC: data samples

The data samples taken at the LHC since 2009 are shown in Table 2.

Table 2. Data samples from LHC

Species	$\sqrt{s_{\mathrm{NN}}}$, GeV
$p + p$	900, 2360, 2760, 5020, 7000, 8000, 13000, 13600
p + Pb	5020, 8160
Xe + Xe	5440
Pb + Pb	2760, 5020

Study of collective effects at LHC

ALICE, ATLAS and CMS are a general-purpose detectors. ALICE is specially conceived and constructed for study with ion, mostly heavy, beams at the LHC. ATLAS and CMS are designed to observe any phenomena within and beyond Standard Model (SM) that the LHC might reveal, including studies of strong interaction from production of particles at low energies and the spectroscopy of hadrons to perturbative QCD with hadronic jets. Designs of all of these detectors are well optimized for study of wide sets of collective effects.

The LHCb detector is designed for precision measurements of CP violation and rare decays of beauty and charm hadrons. The LHCb observes the particles thrown forward by a collision. Nevertheless the LHCb is single-arm spectrometer an important results have been already obtained for femtoscopic correlations and jet physics with this apparatus.

Emergence of hadronic jet

Collisions of protons and nuclei at high enough energies often engender hard scatterings which lead to the formation of hard partons, with energies $E >> Q$ the virtuality of the parton. At high enough energy, the virtuality Q is itself much larger than Λ_{QCD} ($Q >> \Lambda_{\text{QCD}}$).

The decay of these hard partons occurs via the repeated emission of progressively softer partons. Due to the condition $E >> Q$, the ensuing spray of partons is collinearly collated into jets of partons which future transforms via hadronization into jets of observable hadrons. The large scales involved allow for the use of pQCD to calculate the cross section and various other properties of these jets.

Jets at high energies

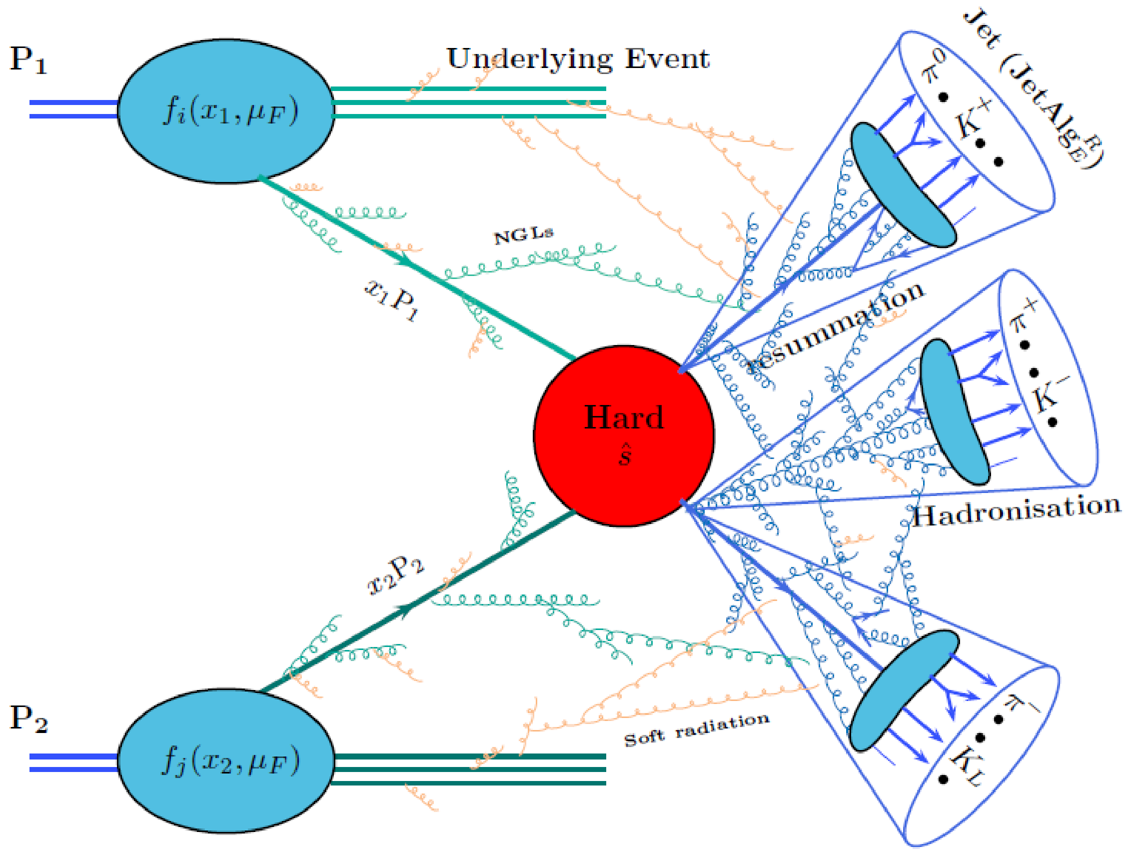

Fig. 7. A typical LHC multijet event with associated various perturbative and non–perturbative effects. Former effects include: hard scattering subprocess, soft and collinear radiation (resummation), soft and wide–angle radiation, non-global logs (NGLs), effects of jet algorithms (JetAlg) with jet radius R and recombination scheme E. Latter effects include: parton densities $f\,(x,\mu_F)$*, underlying event (UE) and hadronisation [6].*

Reconstruction of hadronic jet

It is important to note that a jet is defined by the jet-finding algorithm used to cluster the resulting fragmentation products into a jet.

The standard set of appropriate kinematic variables consists of the transverse momentum (p_{T}), rapidity (y) or pseudorapidity (η), azimuthal angle (ϕ), and invariant mass (m_{j}) of the jet. At present there are two most popular families of algorithms for jet funding, namely,

– cone algorithms

and

– k_{T} algorithms.

In both cases the distance parameter ΔR_{ij} (or, in other notations, ΔR, R_{ij}, R)

$$\Delta R_{ij}^2 = (\eta_i - \eta_j)^2 + (\phi_i - \phi_j)^2 \equiv (\Delta\eta)^2 + (\Delta\phi)^2$$

is introduced in the η–ϕ plane in order to cluster each pair of objects i and j into a jet.

Inclusive jets and dijets

In $p+p$ collisions the inclusive jet cross sections are measured double-differentially as a function of the jet transverse momentum (p_T) and rapidity (y). The double-differential dijet production cross sections are presented as a function of the dijet mass (m_{jj}) and the half absolute rapidity separation between the two leading jets.

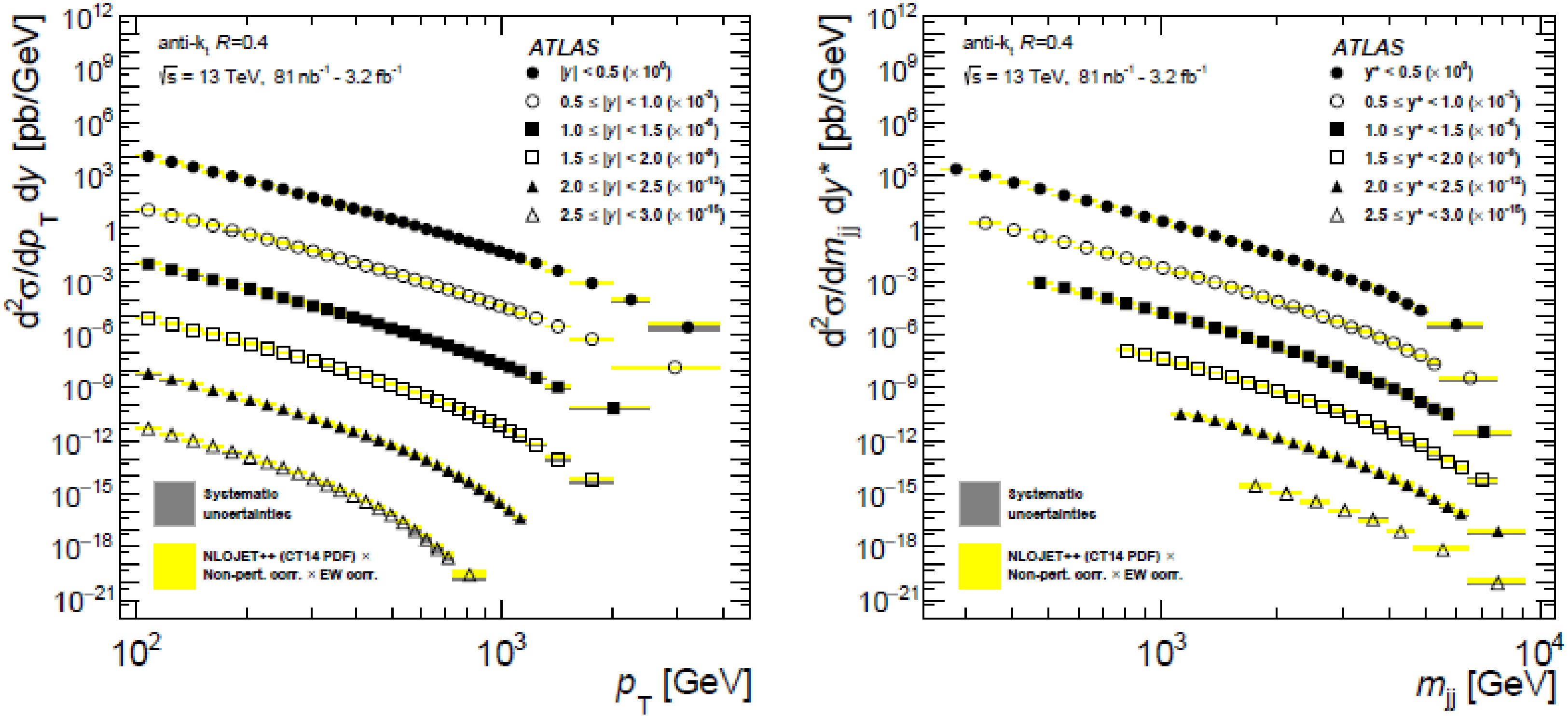

Fig. 8. The measured inclusive jet (left) and inclusive dijet (right) cross-sections at $\sqrt{s}$ = 13 TeV, shown as a function of the jet p_T or dijet m_{jj} in several jet rapidity bins [7].

Experiment vs theory

Overall, fair agreement between the measured cross sections (that span several orders of magnitude) and the fixed-order NNLO pQCD calculations, corrected for non-perturbative and electroweak effects, is observed (Fig. 8). However, when considering data points from all jet transverse momentum and rapidity regions in the inclusive jet measurement, a some discrepancy between data and theory is observed. Resolving this issue requires a good understanding of the correlations of the experimental and theoretical systematic uncertainties in jet p_T and rapidity.

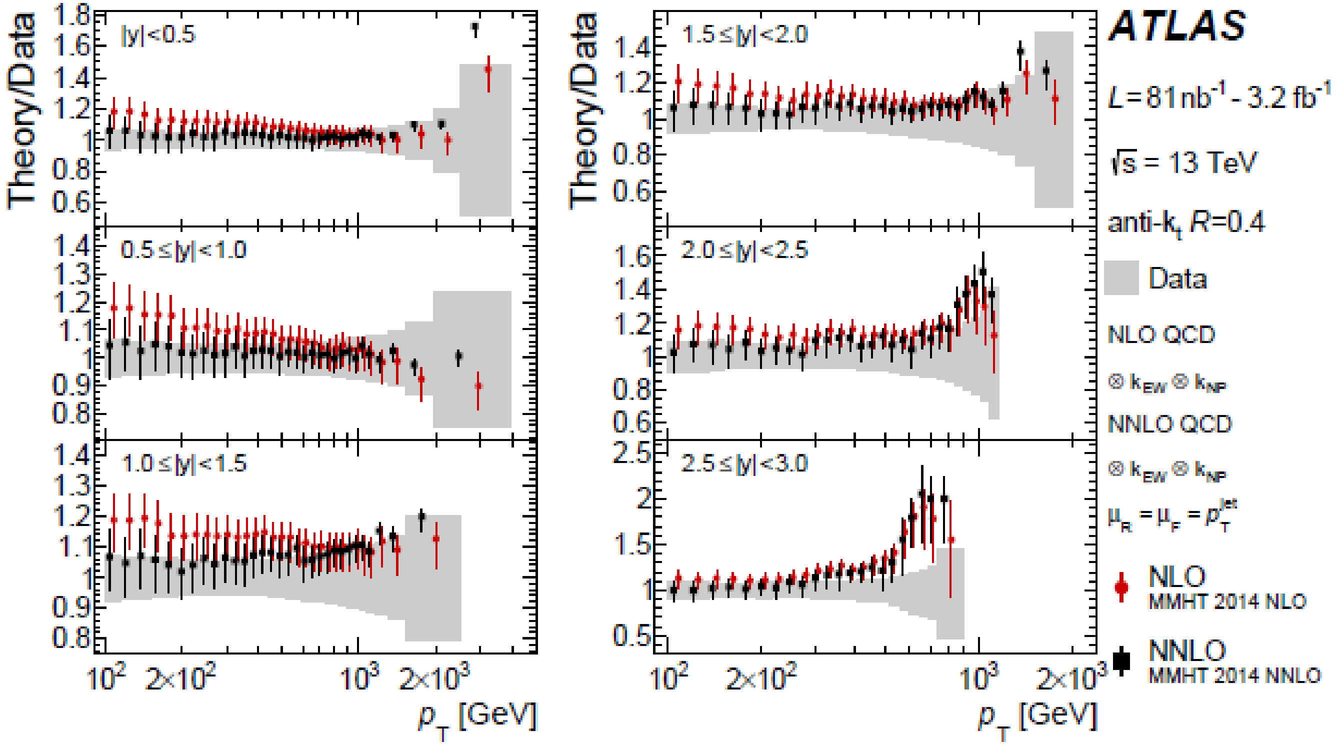

Fig. 9. The ratios of NLO and NNLO pQCD predictions to the measured inclusive jet cross sections. The theory uncertainties are shown by the lines and the shaded bands show the total data uncertainty including both the systematic and statistical uncertainties [7].

Q-Evolution of α_S

The evolution of the strong coupling as a function of the energy scale, $\alpha_S(Q)$ has been tested with help of the ratio observable $R_{\Delta\phi}(p_T)$, related to the azimuthal correlations among jets up to $Q \approx 2$ TeV, a higher scale than that probed in previous measurements. This test has been performed by choosing as energy scale Q the average jet p_T in the different intervals considered, and no deviation from the expected NLO pQCD running of the strong coupling is observed.

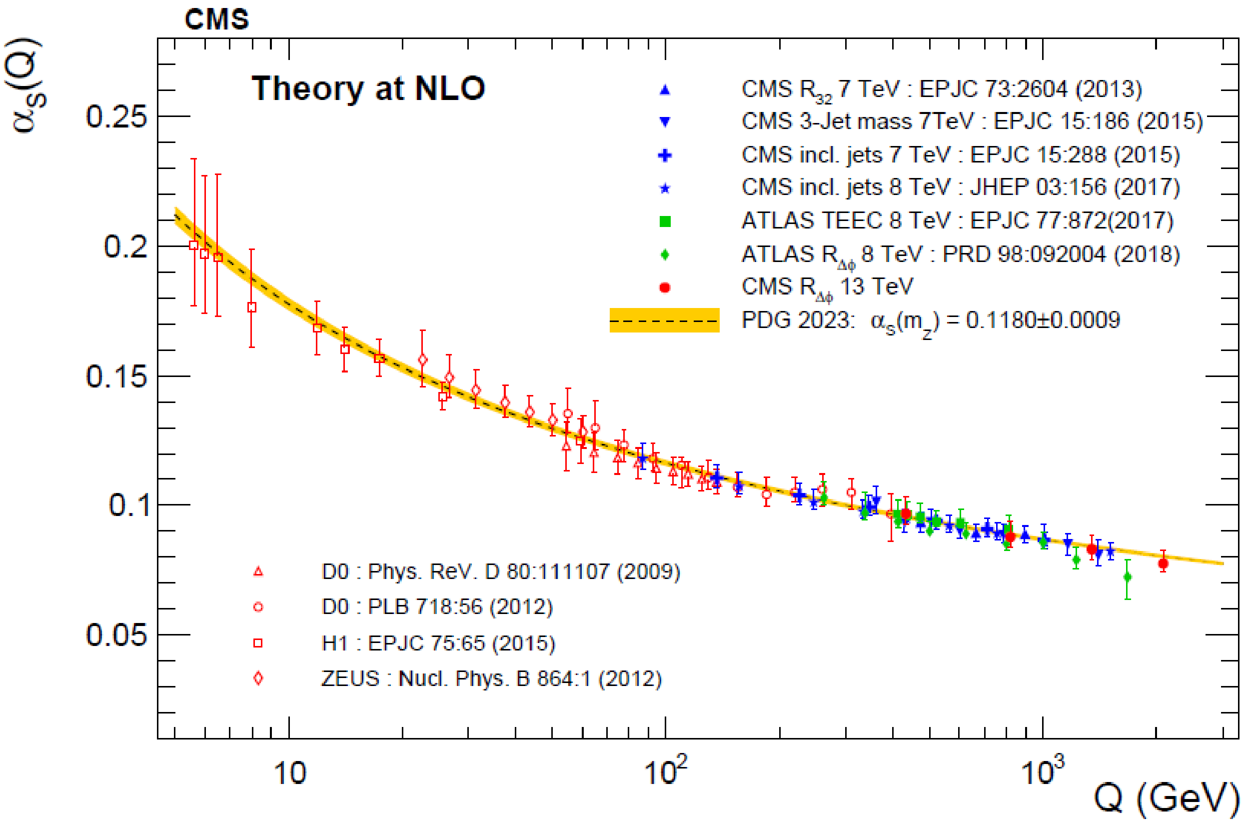

Fig. 10. Running of the strong coupling $\alpha_S(Q)$ (dashed line) evolved using the current world-average value $\alpha_S(m_Z) = 0.1180 \pm 0.0009$ [8] together with its associated total uncertainty (yellow band). The vertical error bars indicate the total uncertainty (experimental and theoretical). All the experimental results shown in this figure are based on fixed-order predictions at NLO accuracy in pQCD [9].

Dead-cone effect in QCD

Studying the pattern of the parton shower is one of the key experimental tools for testing QCD. The dead-cone effect predicts a suppression of the gluon spectrum emitted by a heavy quark of mass m_Q and energy E, within a cone of angular size m_Q / E around the emitter.

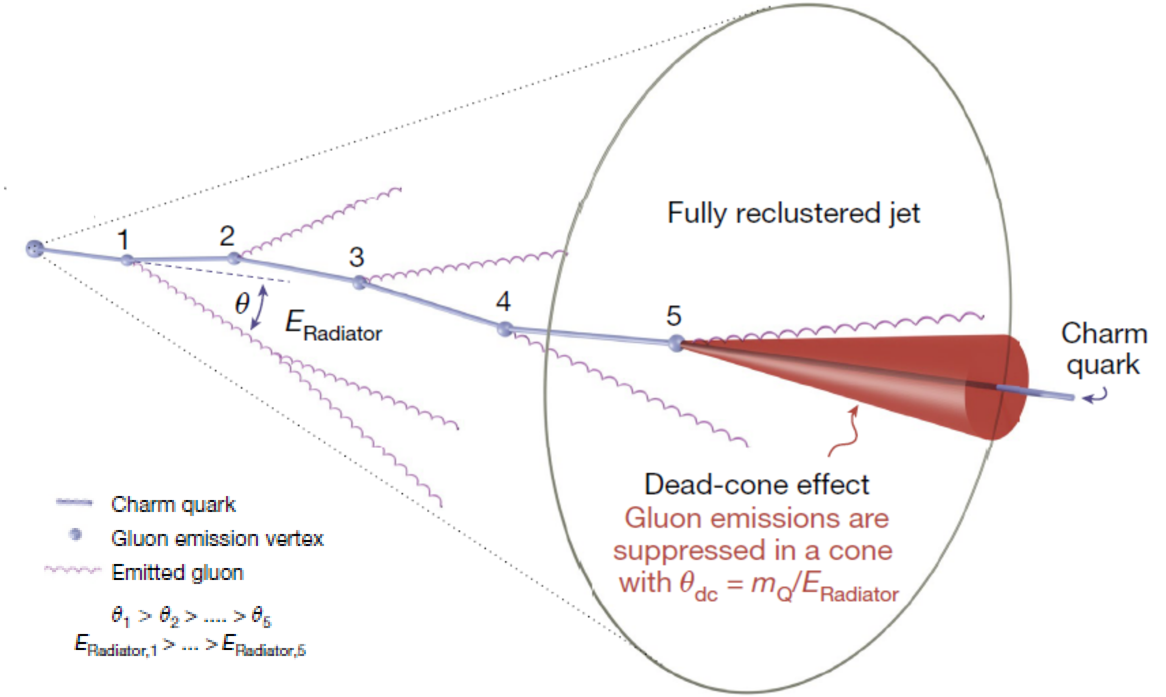

Fig. 11. A sketch for creation of the dead cone in QCD. With each splitting, the c-quark energy, $E_{Radiator,n}$, is reduced and the gluon is emitted at a smaller angle, θ_n, with respect to previous emissions. The mass of the heavy quark, m_Q, remains constant throughout the showering process. At each splitting, gluon emissions are suppressed in the dead-cone region (shown by a red cone for the last splitting), which increases in angle as the quark energy decreases throughout the shower [10].

$R(\theta)$ observable

The observable used to reveal the dead cone is built by constructing the ratio of the splitting angle (θ) distributions for D^0-meson tagged jets and inclusive jets, in bins of E_{Radiator}. This is given by

$$R(\theta) = \frac{1}{N^{\mathrm{D^0\,jets}}} \frac{dn^{\mathrm{D^0\,jets}}}{d\ln(1/\theta)} \Big/ \frac{1}{N^{\mathrm{inclusive\;jets}}} \frac{dn^{\mathrm{inclusive\;jets}}}{d\ln(1/\theta)} \Bigg|_{k_{\mathrm{T}},\, E_{\mathrm{Radiator}}}$$

where the θ distributions were normalized to the number of jets that contain at least one splitting in the given E_{Radiator} and k_{T} selection, denoted by $N^{\mathrm{D0\;jets}}$ and $N^{\mathrm{inclusive\;jets}}$ for the D^0-meson tagged and inclusive jet samples, respectively. In the absence of mass effects, the c quark is expected to have the same radiating properties as a light quark. In this limit, above equation can be re-written as

$$R(\theta)_{\mathrm{no\;dead\text{-}cone\;limit}} = \frac{1}{N^{\mathrm{LQ\;jets}}} \frac{dn^{\mathrm{LQ\;jets}}}{d\ln(1/\theta)} \Big/ \frac{1}{N^{\mathrm{inclusive\;jets}}} \frac{dn^{\mathrm{inclusive\;jets}}}{d\ln(1/\theta)} \Bigg|_{k_{\mathrm{T}},\, E_{\mathrm{Radiator}}}$$

where the superscript LQ refers to light quarks, and the inclusive sample contains both light-quark and gluon-initiated jets. In the limit of having no dead-cone effect, the ratio of the θ distributions for D^0-meson tagged jets and inclusive jets becomes $R(\theta)_{\mathrm{no\;dead\text{-}cone\;limit}} > 1$, at small angles.

$R(\theta)$ in $p+p$ collisions

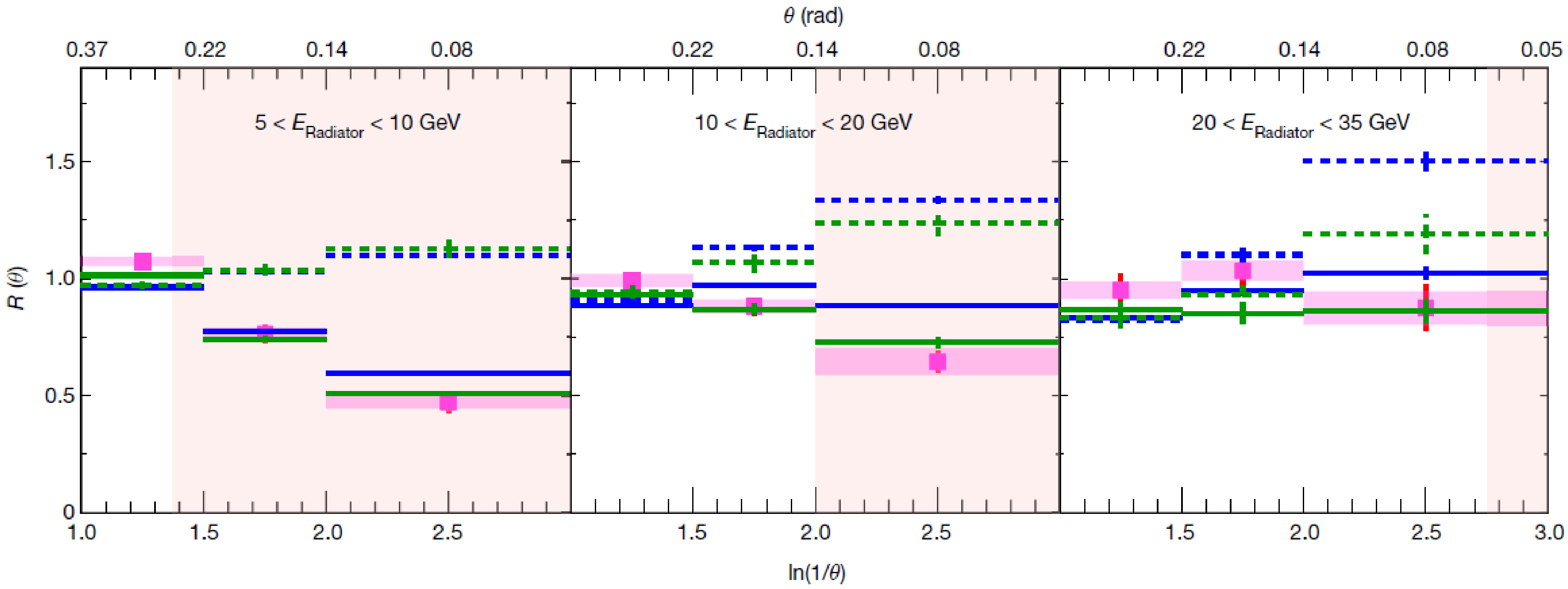

Fig. 12. The ratios of the splitting angle probability distributions for D^0-meson tagged jets to inclusive jets, $R(\theta)$, measured in p+p collisions at $\sqrt{s} = 13$ TeV, are shown by points for $5 < E_{Radiator} < 10$ GeV (left), $10 < E_{Radiator} < 20$ GeV (middle) and $20 < E_{Radiator} < 35$ GeV (right). The data are compared with PYTHIA v.8 (blue lines) and SHERPA (green lines) simulations, including the no dead-cone limit given by the ratio of the angular distributions for light-quark jets (LQ) to inclusive jets (dashed lines). The pink shaded areas correspond to the angles within which emissions are suppressed by the dead-cone effect, assuming a $m_c = 1.275$ GeV/c^2 [10].

Dead-cone effect for *c* quark

A lower limit for the significance of the small-angle suppression is estimated by comparing the measured data to $R(\theta) = 1$, which represents the limit of no dead-cone effect in the case in which the inclusive sample is entirely composed of light quark-initiated jets. The significances of the results in dependence of the energy of radiator, i.e. *c* quark, are summarized in Table 3.

Table 3. Significance of the results

Range of E_{Radiator}, GeV	Significance, σ
$5 < E_{\text{Radiator}} < 10$	7.7
$10 < E_{\text{Radiator}} < 20$	3.5
$20 < E_{\text{Radiator}} < 35$	1.0

One can note that a σ value greater than 5 is considered the criteria for a definitive observation, whereas the value of 1.0 is consistent with the null hypothesis.

These results pave the way for a study of the mass dependence of the dead-cone effect, by measuring the dead cone of beauty jets tagged with a reconstructed beauty hadron. This measurement provides direct sensitivity to the mass of quasi-free charm quarks, before they bind into hadrons.

Nuclear modification factor

The nuclear modification factor R_{AA} is the ratio of the number of some objects (particles, jets) measured in A+A collisions to the yield in p+p collisions scaled by the average number of binary nucleon-nucleon collisions.

$$R_{AA}(p_T)=\frac{1}{\langle N_{\mathrm{bin}}\rangle}\frac{d^2N^{AA}/dp_Td\eta}{d^2N^{pp}/dp_Td\eta}=$$

$$=\frac{1}{\langle N_{\mathrm{bin}}\rangle/\sigma_{\mathrm{inel}}^{pp}}\frac{d^2N^{AA}/dp_Td\eta}{\sigma_{\mathrm{inel}}^{pp}d^2N^{pp}/dp_Td\eta}=$$

$$=\frac{1}{T_{AA}}\frac{d^2N^{AA}/dp_Td\eta}{d^2\sigma^{pp}/dp_Td\eta},$$

where T_{AA} is the nuclear overlap function.

R_{AA} for jets

Experiments at the LHC extend the measurements for jet quenching up to $p_T \approx 1$ TeV/c. Jet R_{AA} exhibits larger suppression than hadrons at the same p_T, with the ALICE jet spectrum extending down to $p_T = 60$ GeV/c. At higher p_T the ALICE and ATLAS jet data are consistent, and show slowly increasing R_{AA} with increasing p_T.

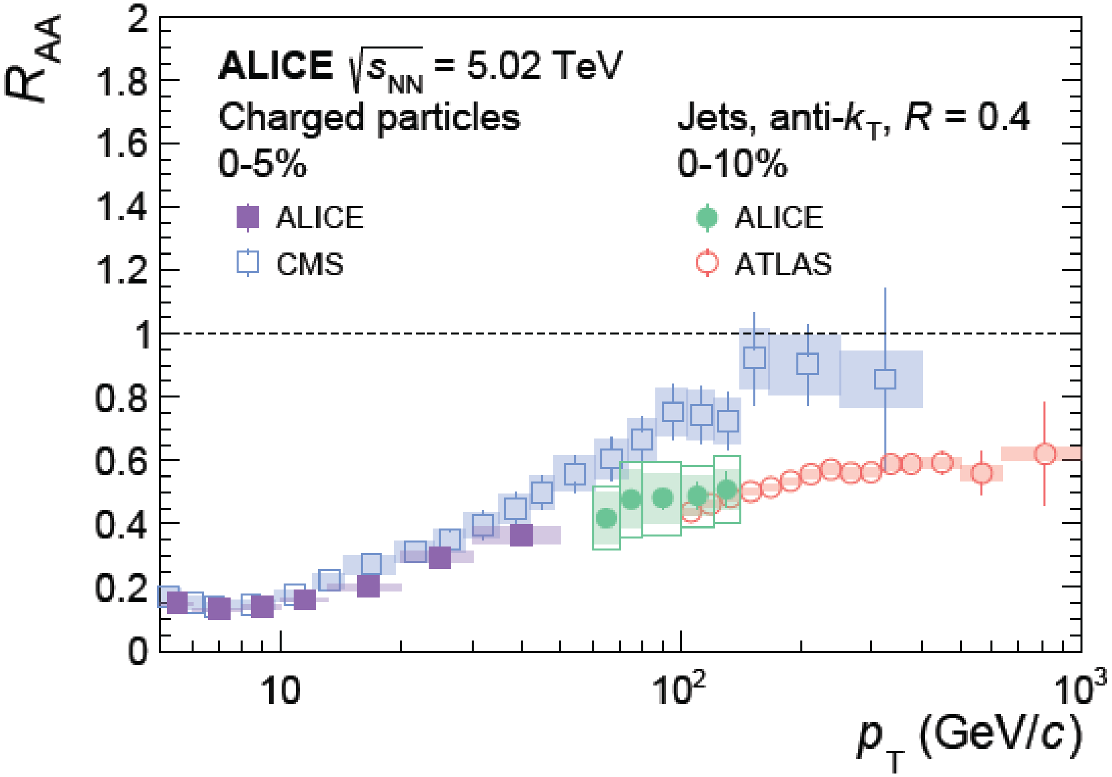

Fig. 13. Measurement of R_{AA} for charged hadrons and jets in central Pb+Pb collisions. A global normalisation uncertainty of 3% on R_{AA} is not shown in the figure. [11].

Heaviest SM particles and QGP

It seems important to remind the following little bit of the Panel Discussion IV: phenomena in heavy ion collisions (Moderator: Serguei Sadovsky)

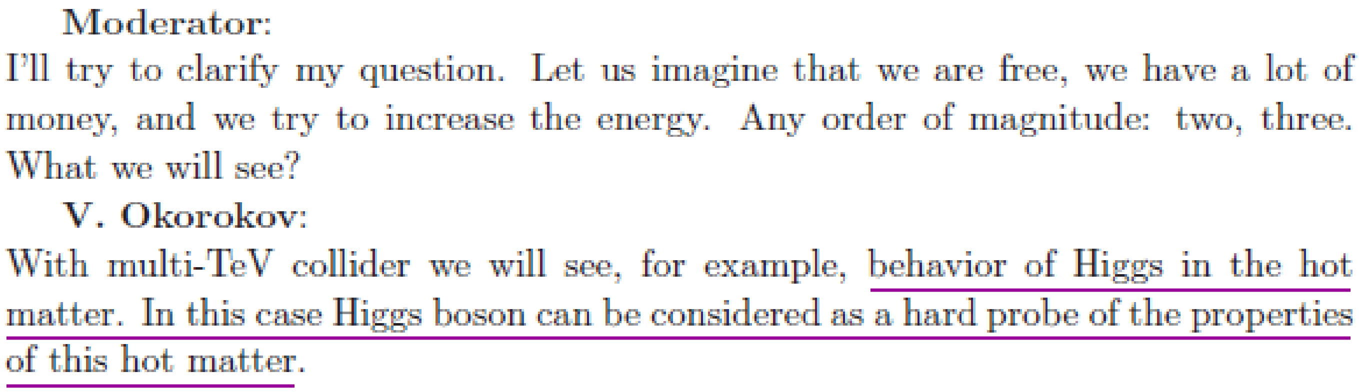

Moderator:
I'll try to clarify my question. Let us imagine that we are free, we have a lot of money, and we try to increase the energy. Any order of magnitude: two, three. What we will see?

V. Okorokov:
With multi-TeV collider we will see, for example, behavior of Higgs in the hot matter. In this case Higgs boson can be considered as a hard probe of the properties of this hot matter.

during XXXth International Workshop on High Energy Physics "Particle and Astroparticle Physics, Gravitation and Cosmology: Predictions, Observations and New Projects" which was held at the Institute for High Energy Physics, Protvino, Russia 23-27 June, 2014 [12].

At present the Higgs boson (*h*) and *t* quark, the heaviest elementary particles known, are widely considered as important probes of a pre-equilibrium stages of space-time evolution of QGP in domain of high (multi-TeV) and ultra-high collision energies [13, 14].

Measurable channel

The dilepton final states, in which both W bosons decay into leptons (l) and the corresponding neutrinos (ν), are the cleanest final states for the antitop-top pair signal measurement, despite their relatively small branching fraction [8]

$$Br(t\overline{t} \rightarrow W^{+}bW^{-}\overline{b} \rightarrow l^{+}\nu_{l}bl^{-}\tilde{\nu}_{l}\overline{b}) = 5.25\%, \quad l^{\pm} = e^{\pm}, \mu^{\pm}.$$

Datasets with large integrated luminosities obtained at the LHC for p+Pb at $\sqrt{s_{\mathrm{NN}}} = 8.16$ TeV and Pb+Pb at $\sqrt{s_{\mathrm{NN}}} = 5.02$ TeV result in the reconstruction of antitop-top events in the

– $l^{+}l^{-}$ + jets

and

– dilepton ($l^{+}l^{-}$)

channels become accessible experimentally, where $l^{+}l^{-} = e^{+}e^{-}, \mu^{+}\mu^{-}, e\mu$.

t Quark in *p*+Pb

In *p*+Pb collisions at $\sqrt{s_{NN}}$ = 8.16 TeV the CMS experiment observed antitop-top pair production using the *l* + jets decay channel; the ATLAS experiment reconstructed that pair in *l* + jets and di-lepton channels using final states with electrons and muons.

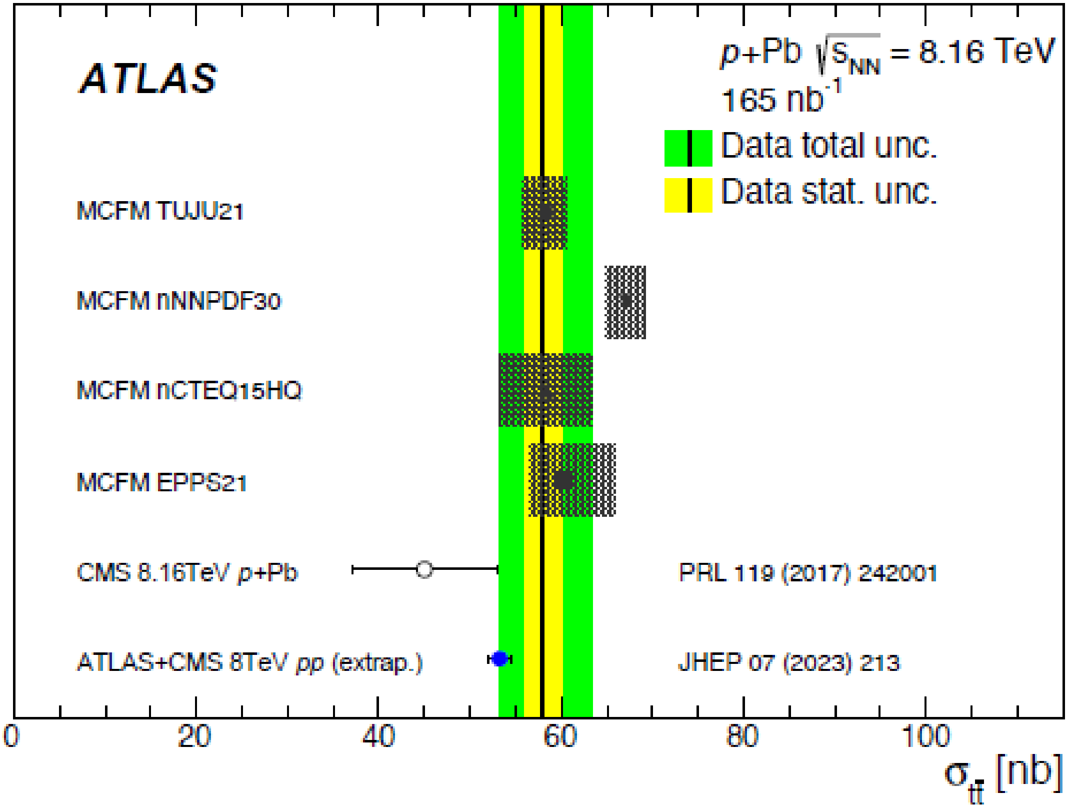

Fig. 14. Comparison between observed and predicted values of cross sections for antitop-top pair production in p+Pb and p+p collisions at close energies. The latter is extrapolated to the $\sqrt{s_{NN}}$ *of p+Pb measurement and also using the* A_{Pb} *factor. The uncertainty on predictions (grey box) represents the uncertainty on internal PDF. The solid black line indicates the measured value. The combined statistical and systematic uncertainty of the measurement is shown in green while the statistical component is depicted in yellow [15].*

t Quark in Pb+Pb

In Pb+Pb collisions at $\sqrt{s_{NN}}$ = 5.02 TeV the CMS experiment observed antitop-top pair production using the *l* + jets and dilepton decay channel.

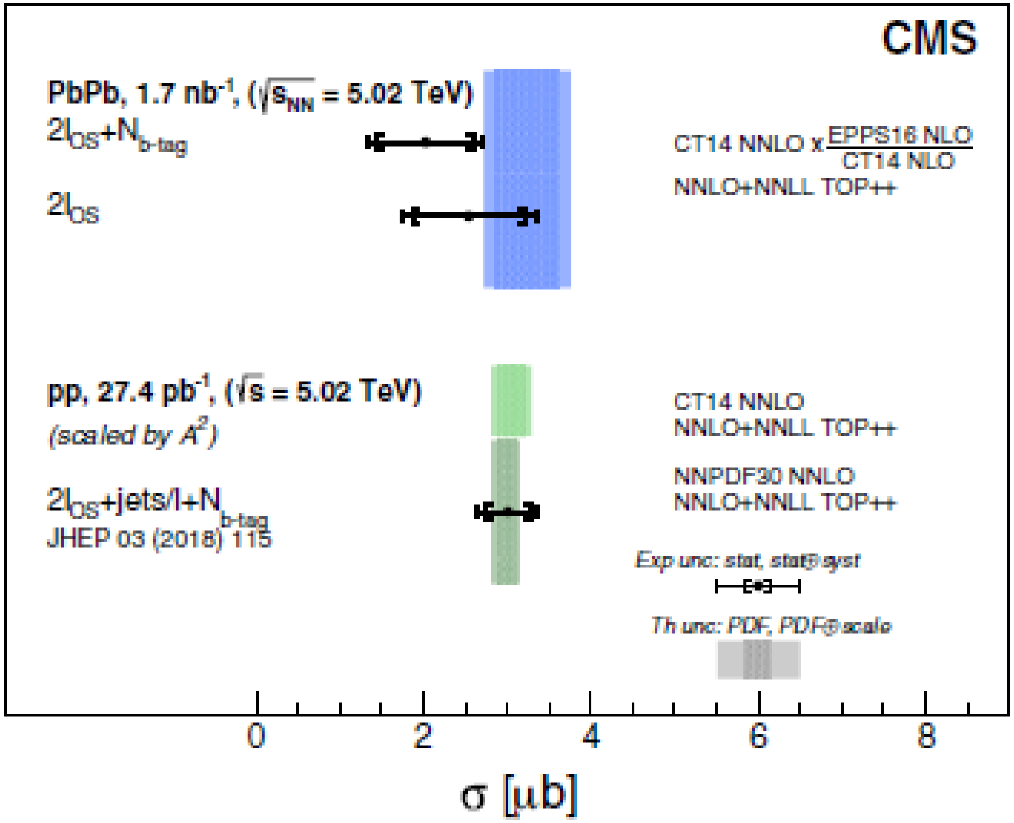

Fig. 15. Inclusive antitop-top pair production cross sections measured with two methods in the combined three lepton final states in Pb+Pb and p+p (scaled by A^2) collisions. The measurements are compared with theoretical predictions at NNLO + NNLL accuracy in QCD. The inner (outer) experimental uncertainty bars include statistical (statistical and systematic, added in quadrature) uncertainties. The inner (outer) theoretical uncertainty bands correspond to nuclear or free-nucleon PDF (PDF and scale, added in quadrature) uncertainties. [16].

Cross sections for antitop-top

For p+Pb at √s$_{NN}$ = 8.16 TeV the most precision result is obtained by ATLAS. Combining both channels, the antitop-top pair production cross section is measured to be

$$\sigma_{\bar{t}t}^{p+Pb} = \left[58.1 \pm 2.0(\text{stat.})\,^{+4.8}_{-4.4}(\text{syst.})\right]\ \text{nb.}$$

Cross sections measured by ATLAS and CMS are found to be in good agreement each other and with SM predictions. Precision of these measurements opens a new way to constraint PDFs in the high-x region.

For Pb+Pb at √s$_{NN}$ = 5.02 TeV the CMS results are

$$\sigma_{\bar{t}t}^{Pb+Pb} = \left[2.5^{+0.8}_{-0.7}\right]\ \mu\text{b};\quad \left[2.0^{+0.7}_{-0.6}\right]\ \mu\text{b}$$

utilizing the leptons only, and in a second method, in addition, the b quarks respectively. This measurement is just the first step in using the t quark as a novel and powerful probe of the QGP.

Emergence of low-Δp correlations

The space-time extents of emissions region of secondary particles (fireball) are of fundamental interest for better understanding of subatomic physics and the evolution of (very) earle Universe. The shape and other properties of fireball can be determined by using the method of momentum correlations in the system of two or more particles at small relative momenta in some reference frame. That is the subject of study within the field of (correlation) femtoscopy.

The correlations at low relative momentum, called also as femtoscopic correlations, emerge due to both the symmetrization requirement of quantum statistics (QS) and the effect of final state interaction (FSI) among particles of the system under consideration. Therefore, in general, the femtoscopic correlations can appear in a system of any (identical or non identical) particles.

Correlation function in experiment

Experimentally, correlation function (CF) in general case of *n*-particle system is defined as the ratio

$$C_n(p_1,\ldots,p_n) = \xi(p_1,\ldots,p_n)\frac{N_{\text{same}}(p_1,\ldots,p_n)}{N_{\text{mixed}}(p_1,\ldots,p_n)}.$$

Here $N_{\text{same}}(p_1,\ldots,p_n)$ and $N_{\text{mixed}}(p_1,\ldots,p_n)$ represent the distributions for particles produced in the same and in different collisions, respectively. The last distribution is the reference one that by construction is expected to include no femtoscopic correlation. The first term in r.h.s. – $\xi(p_1,\ldots,p_n)$ – denotes the corrections for all experimental effects (acceptance, particle identification etc.).

At present two- ($n = 2$) and three-body ($n = 3$) systems are mostly considered in femtoscopy on point of view of experiment as well as phenomenology.

Space-time extents of source

The correlations of identical particles with low relative momenta are mostly used for study of space-time extents of fireball. The main part of experimental data are obtained for pairs of charged pions, there are some results for (anti)*p* – (anti)*p*, neutral particle (γ, π, *K*, Λ) and charged kaon pairs.

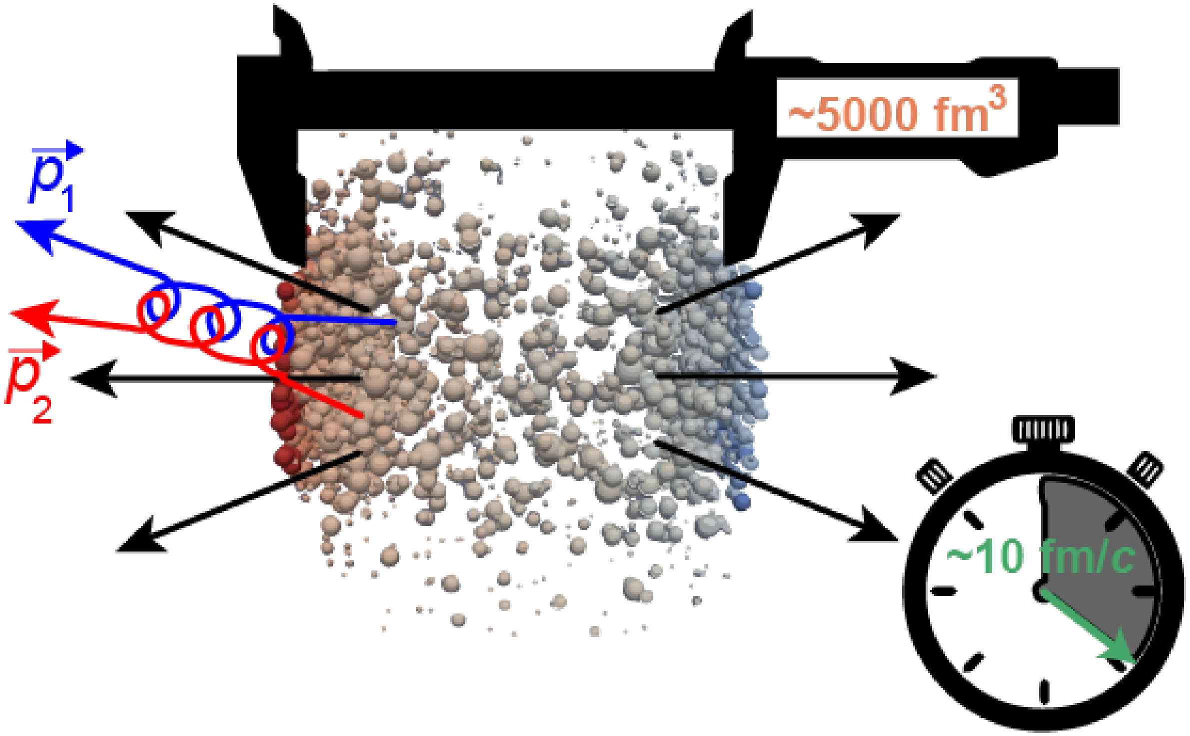

Fig. 16. Schematic view of the source of secondaries and order of magnitude for the volume of emission region and time duration until kinetic freeze-out stage in heavy ion collisions at the LHC [17].

Study of *h–h interactions*

The study of the residual strong interaction among hadrons (*h*–*h*) is still an open topic in nuclear physics. This also has implications for relativistic astrophysics. The FSI effect allows for the correlation femtoscopy with unlike particles the access, in particular, to a study of strong interactions between specific particles. This issue is in the focus below.

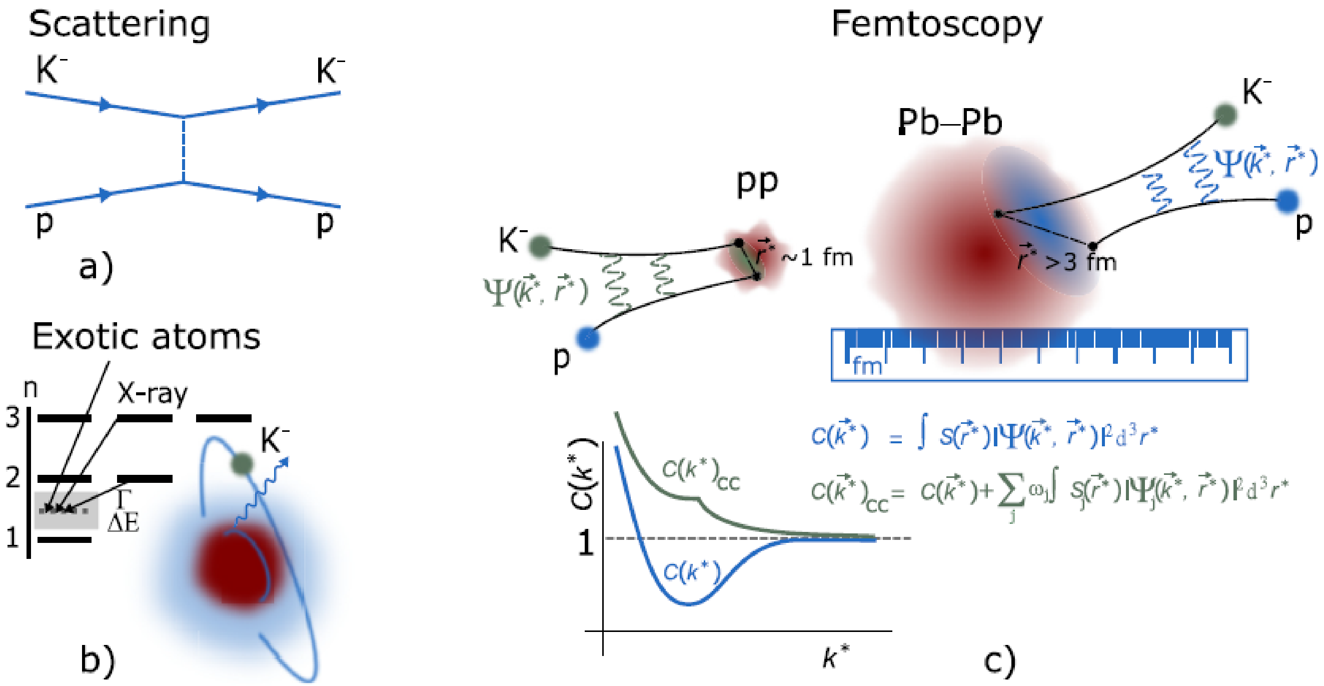

Fig. 17. Schematic illustration of available experimental techniques for measuring the interaction among hadrons: a) scattering experiments, b) measurements of energy shifts from the X-ray de-excitation spectrum of exotic atoms, c) femtoscopy in small collision systems (p+p) with coupled channel effects shown in green, and in large collision systems (Pb+Pb) with vanishing coupled channel contributions shown in blue [18].

Two-body systems (1)

The non identical particle pairs recently studied with help of femtoscopic correlations are shown in Table 4.

Table 4. Femtoscopic analyses for non-id particle pairs

Particle pair	$\sqrt{s_{NN}}$, TeV	Species	Experiment
(anti)p – (anti)Ω	13, 0.20	$p + p$, Au + Au	ALICE, STAR
$\pi^{\pm} - K_S^0$	13	$p + p$	ALICE
$K_S^0 - K^{\pm}$	5.02, 13		
$K^+ - K^-$	2.76	Pb + Pb	
$p - K^+ \oplus$ anti $p - K^-$	5.02	$p + p$, p + Pb, Pb + Pb	
$p - K^- \oplus$ anti $p - K^+$			
$p - K^+ \oplus$ anti $p - K^-$	7, 13	$p + p$	
$p - K^- \oplus$ anti $p - K^+$			
$p - \phi \oplus$ anti $p - \phi$	13		
$p - \Lambda \oplus$ anti p – anti Λ	7, 13		
$p - \Sigma^0 \oplus$ anti p – anti Σ^0	13		
$p - \Xi$			

Two-body systems (2)

Table 4 (continue). Femtoscopic analyses for non-id particle pairs

Particle pair	$\sqrt{s_{NN}}$, TeV	Species	Experiment
$\pi^- - D^{(*)+} \oplus \pi^+ - D^{(*)-}$	13	$p + p$	ALICE
$\pi^- - D^{(*)-} \oplus \pi^+ - D^{(*)+}$			
$K^- - D^{(*)+} \oplus K^+ - D^{(*)-}$			
$K^- - D^{(*)-} \oplus K^+ - D^{(*)+}$			
$p - D^- \oplus$ anti $p - D^+$			
$\Lambda - K^+ \oplus$ anti $\Lambda - K^-$			
$\Lambda - K^- \oplus$ anti $\Lambda - K^+$			
$\Lambda - \Xi$			
$K^+ - d \oplus K^- -$ anti d			
$p - d \oplus$ anti $p -$ anti d			
$p - \Xi^- \oplus$ anti $p - \Xi^+$	5.02	p + Pb	
$\Lambda - K^+ \oplus$ anti $\Lambda - K^-$	2.76	Pb + Pb	
$\Lambda - K^- \oplus$ anti $\Lambda - K^+$			
$(\Lambda \oplus$ anti $\Lambda) - K_S^0$			

$p-\Xi$ interaction

The strong potentials were predicted by the HAL QCD Collaboration for the four allowed spin and isospin states of the $p-\Xi^-$ system. One can see that for all cases, an attractive interaction and a repulsive core characterize the potentials. All the potentials shown in Figure are similar at interparticle distances above 1.5 fm, but the corresponding CFs are very different. This difference is due to the sensitivity of the method to the small distances (below 1 fm) that are typical for $p+p$ and p+Pb collisions.

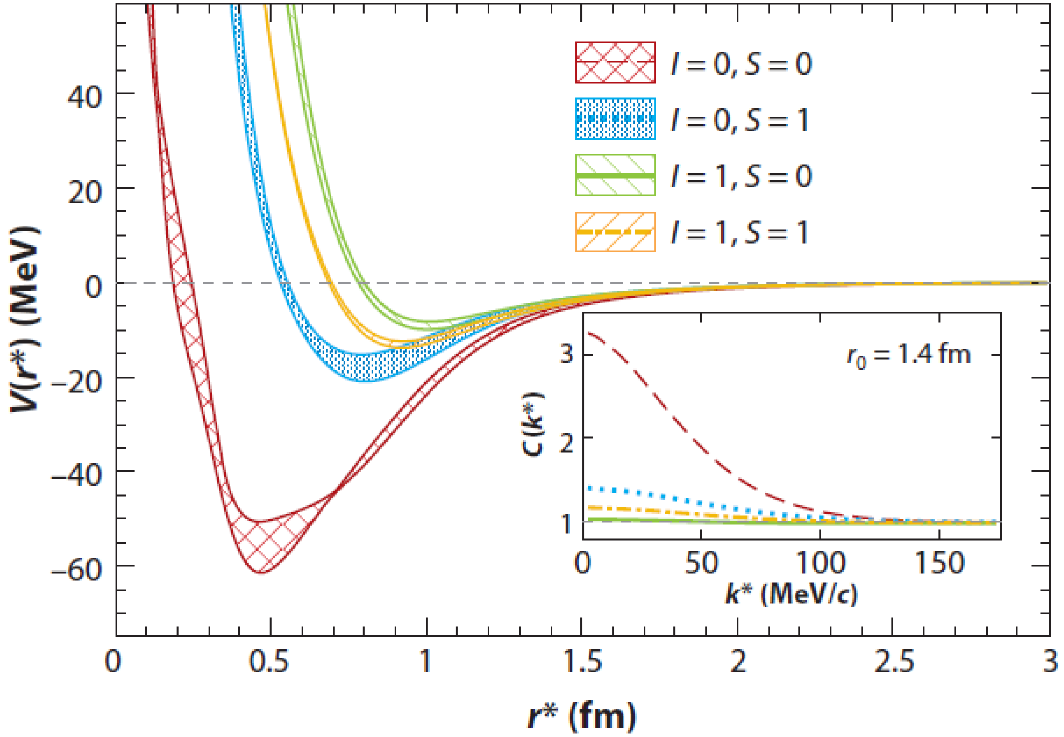

Fig. 18. Strong potentials for the different spin and isospin configurations of the $p-\Xi$ interaction as a function of the interparticle distance. The error bands refer to different Euclidean times considered in the calculation. The inset shows the corresponding CF, which have been evaluated using a Gaussian source with a radius of r_0 = 1.4 fm [19].

V.A. Okorokov
23.07.2024

p–Ξ correlations

The total p–Ξ^- correlation [20] lies above the Coulomb predictions, demonstrating the presence of an additional attractive strong interaction. These data provide a reference that can now be employed to test any theoretical calculation of the p–Ξ^- interaction.

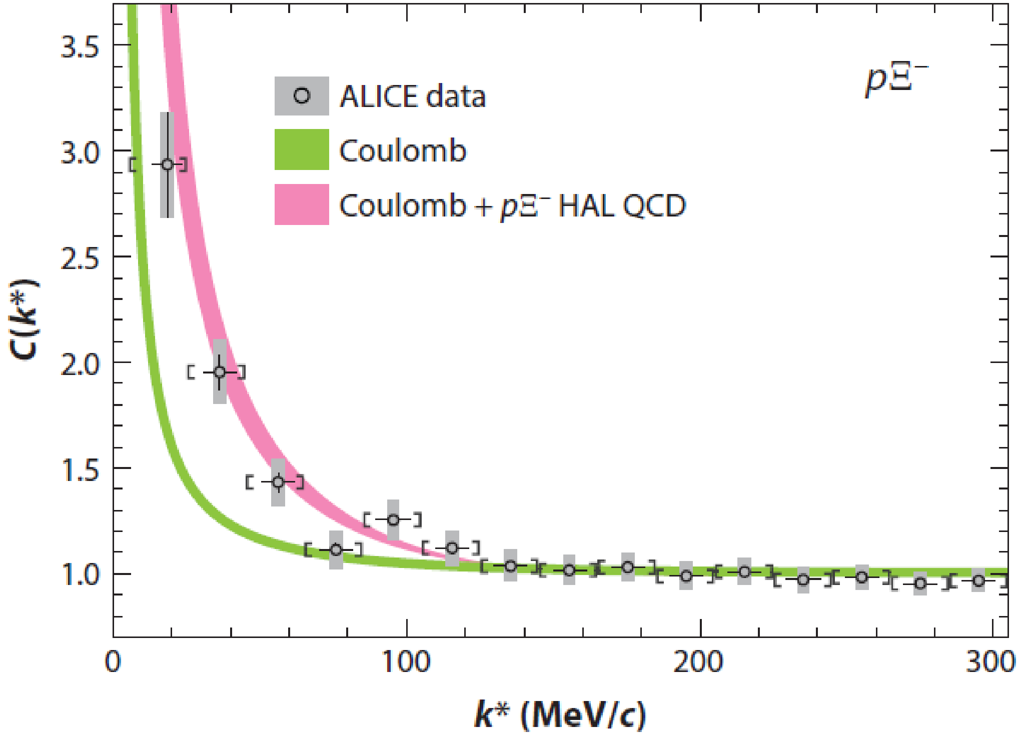

Fig. 19. The $p-\Xi^-$ CF measured in $p+p$ collisions at $\sqrt{s} = 13$ TeV recorded with a high-multiplicity trigger. The experimental data are shown by open circles; error bars indicate statistical errors, and gray boxes indicate systematic errors. The green curve represents the predicted CF assuming only the Coulomb interaction. The pink curve shows the prediction obtained considering the Coulomb and strong interaction provided by the HAL QCD Collaboration [19]. Here k^* is the absolute value of relative 3-momentum of one of the particles in the pair rest frame.

p–Ω interaction

The (anti)p–(anti)Ω CF measured by STAR experiment in Au + Au collisions at $\sqrt{s_{NN}} = 0.2$ TeV includes three effects coming from the elastic scattering in the $^5S_2$ channel, the strong absorption in the $^3S_1$ channel and the long-range Coulomb interaction.

The model-dependent predictions for (anti)p–(anti)Ω CF are based on the p–Ω interaction potential [21]

$$V(r) = b_1 \exp(-b_2 r^2) + b_3 \left[1 - \exp(-b_4 r^2)\right] \left[\frac{\exp(-b_5 r)}{r}\right]^2$$

three versions of which – V_i, $i = I, II, III$ – represent cases without $N\Omega$ bound state (V_I), with a shallow $N\Omega$ bound state (V_{II}) and with deep $N\Omega$ bound state (V_{III}) in dependence of values of free parameters b_i, $i = 1 – 4$.

p–Ω correlations

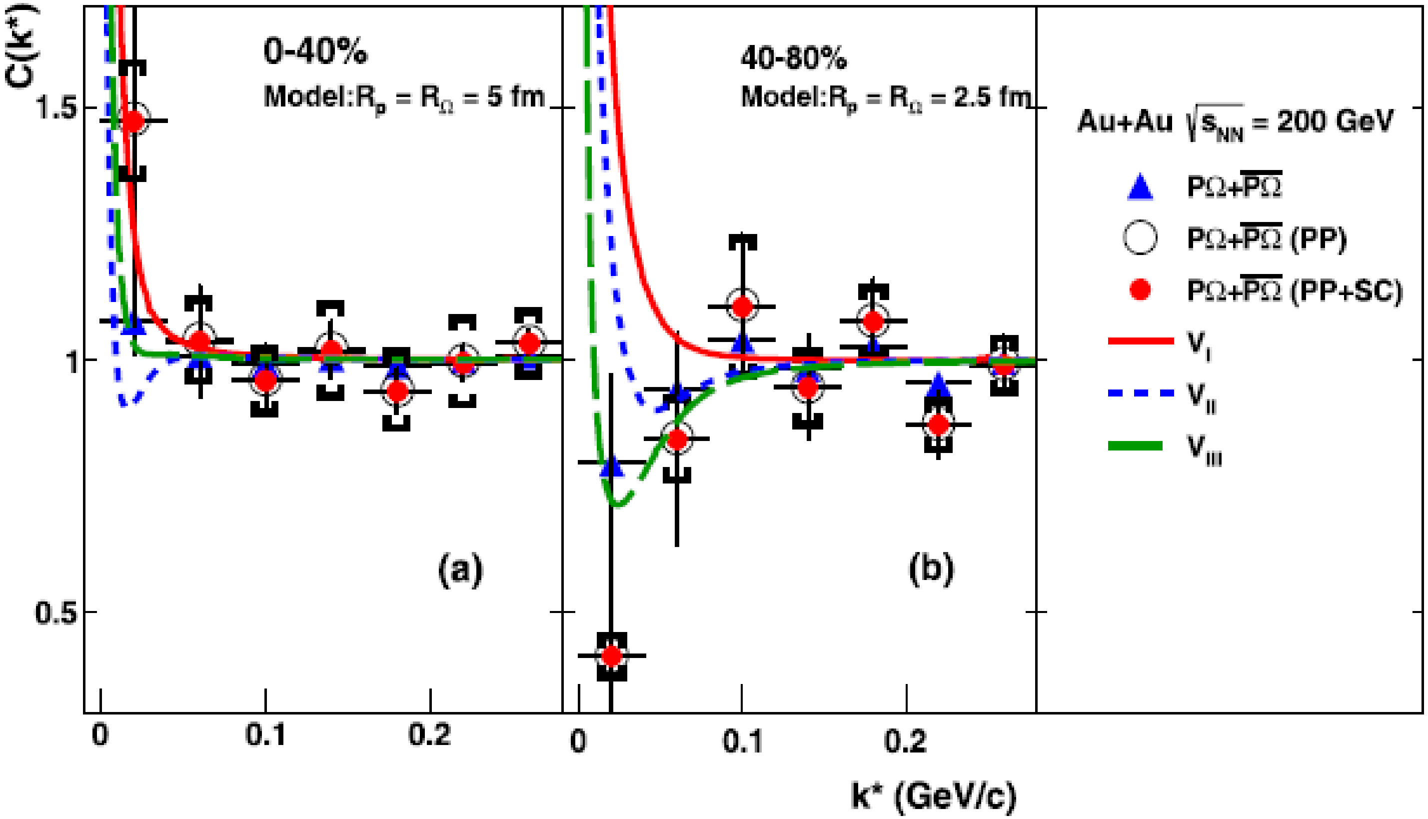

Fig. 20. Measured CF, C(k), for (anti)p–(anti)Ω for (0–40)% (a) and (40–80)% (b) Au+Au collisions at $\sqrt{s_{NN}}$ = 200 GeV. The triangles represent raw correlations, open circles represent pair-purity corrected (PP) correlations, and solid circles represent pair-purity and smearing corrected (PP+SC) correlations. The error bars correspond to statistical errors and caps correspond to the systematic errors. The predictions for various p–Ω interaction potentials are shown for source sizes $R_p = R_\Omega$ = 5 fm (a) and $R_p = R_\Omega$ = 2.5 fm (b) [21].*

Results for p–Ω

At present, due to limited statistics in Au + Au collisions at $\sqrt{s_{NN}} = 0.2$ TeV, it is not possible to extract the interaction parameters.

However, based on the comparison of experimental results and model predictions for CF, one can conclude that data obtained by STAR favor a positive scattering length for the p–Ω interaction. The positive scattering length and the measured ratio of the p–Ω CF from peripheral to central collisions less than unity for $k^{*} < 40$ MeV/c within 1σ favors the p–Ω interaction potential V_{III} with binding energy $E_{\mathrm{b}} \sim 27$ MeV for p and Ω [21], i.e. suggests deep $p\Omega$ bound state.

Three-body systems

The three-body systems of non identical particles recently studied with help of femtoscopic correlations are shown in Table 5.

Table 5. Femtoscopic analyses for three-body systems of non-id particles

Particle system	$\sqrt{s_{NN}}$, TeV	Species	Experiment
$p-(p-\Lambda)$	13	$p+p$	ALICE
$p-(p-\Lambda)\oplus$ anti $p-($anti $p-$ anti $\Lambda)$			
$(p-p)-K^{+}\oplus($anti $p-$ anti $p)-K^{-}$			
$(p-p)-K^{-}\oplus($anti $p-$ anti $p)-K^{+}$			
$p-(p-K^{+})\oplus$ anti $p-($anti $p-K^{-})$			
$p-(p-K^{-})\oplus$ anti $p-($anti $p-K^{+})$			

Implication for NS

Knowledge regarding the interaction of hyperons with nucleons is one of the key ingredients needed to understand the composition of the most dense objects in our universe: neutron stars (NSs).

The high-density environment ($\rho \approx 3\text{–}4\rho_0$) that is supposed to occur in the interior of NSs leads to an increase in the Fermi energy of the nucleons, translating into the appearance of new degrees of freedom, such as hyperons. The inclusion of hyperons leads to NS configurations that cannot reach the current highest mass limit from experimental observations of $2.2M_\odot$. For this reason, the presence of hyperons inside the inner cores of NSs is still under debate, and this so-called hyperon puzzle is far from being solved [19].

Femtoscopy and hyperon puzzle

A major advance in understanding the role played by heavier strange hadrons in the hyperon puzzle has been achieved by the validation of lattice QCD predictions for the $N\Xi$ interaction. As shown above, the measurement of the p–Ξ^- correlation [20] confirmed a strong attractive interaction between these two hadrons and provided a direct confirmation of lattice potentials. Using this same interaction as a starting point to extrapolate results in a neutron-rich dense system, one can obtain a repulsive average interaction of roughly +6 MeV.

M(*R*) with recent constraints

Figure shows the resulting dependence $M(R)$ obtained with EoS taking into account aforementioned experimental results for p–Ξ correlations. This EoS allows the existence of heavy NS with $M > 2M_\odot$ at radii within the narrow range 11.5–12.5 km, which is fully compatible with the recent measurements of NSs close to and above two solar masses.

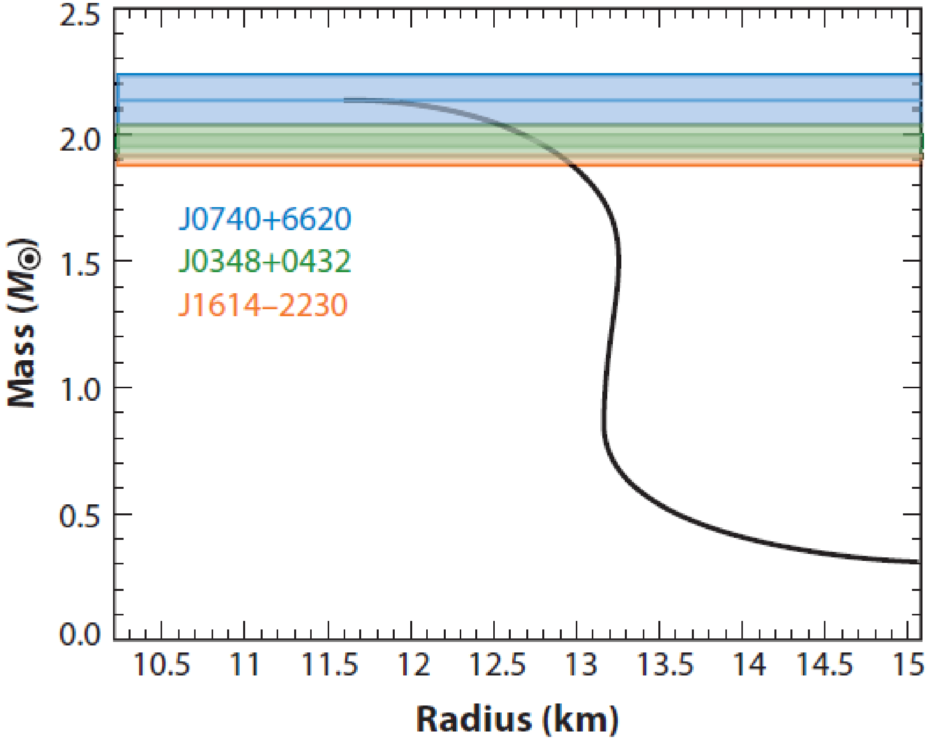

Fig. 21. Mass–radius relation-ship for the EoS scenario taking into account the constraints from the recent accelerator data for p–Ξ interaction. The astrophysical measurements of heavy NSs are shown by the orange, green, and blue bands [19].

Condensation in general case

System with arbitrary number of bosons can undergo a Bose–Einstein condensation (BEC) due to statistical properties of quantum system and symmetry of the wave function of a boson state. In particular, in condensed matter physics, a Bose–Einstein condensate is a state of matter under some conditions, in which large fraction of bosons occupy the lowest quantum state. It is important to note in that state microscopic quantum mechanical phenomena, particularly wave function interference, become apparent macroscopically [22].

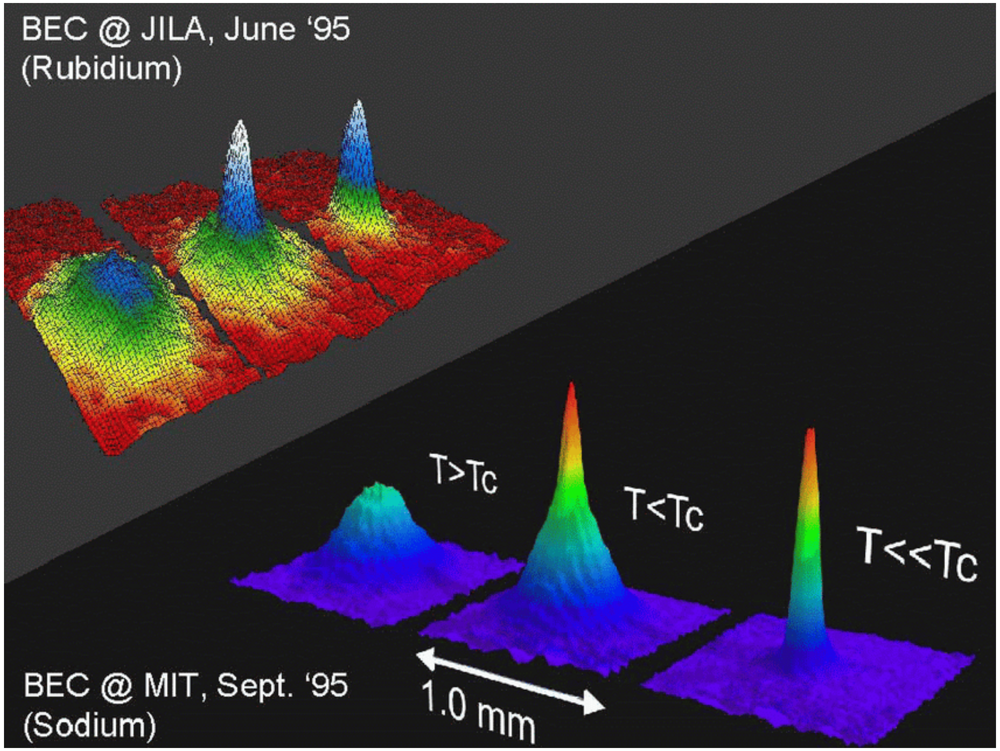

Fig. 22. Experimental observation of Bose–Einstein Condensation in ^{87}Rb at JILA (above) and in ^{23}Na at MIT (below). In both pictures, the left frame represents the gas at a temperature just above the critical condensation temperature, the center frame the same gas just after the condensation and the right frame a nearly pure condensate. The upper picture is a computer image of the momentum distribution, the lower one of the spatial distribution [23].

Why study BEC

Bose–Einstein condensates responsible for laser, superfluids and superconductors.

System with arbitrary number of bosons can undergo a Bose–Einstein condensation

(a) either by cooling,

(b) or increasing the number density of bosons,

(c) or by increasing the overlap of the multi-boson wave-packet states, achieved by changing the size of the single-particle wave-packets.

Regarding the multiparticle production process the mechanisms (b) and (c) lead to condensation of bosons into the same quantum state and bosonic (pion) laser could be created [24–26].

Space density of charged particles

The particle density is defined as follows:

$$n_{ch} = N_{ch} / V,$$

where N_{ch} is the total charged particle multiplicity, V – estimation for the volume of the emission region of the boson under consideration (pions).

The critical value for n_{ch} can be calculated with help of the equation above and transition to the critical total multiplicity. Also one can note the physical quantities in r.h.s. of the above equation – N_{ch} and V – are model-dependent.

The equation for the critical value of N_{ch} for 3D case was suggested elsewhere [27] based on the model for 1D thermal Gaussian distribution. Application of the equation from [27] to the energy domain 10^{17}–10^{21} eV shown the possibility of Bose–Einstein condensation at least for nuclear interactions with ultra-high energy cosmic ray (UHECR) particles [28].

Critical total multiplicity

Based on the generalized of the pion-laser model for the case of overlapping wave packets with complete n–particle symmetrization in our work [29] the following equation for the critical value of N_{ch} for 3D case is suggested

$$N_{ch}^{c} = \eta^{-1}\left[\frac{1+X+\sqrt{X+1}}{2}\right]^{3/2}, \quad X \equiv 2mT_{\text{eff}}R_{\text{eff}}^{2};$$

$$T_{\text{eff}} = T + \Delta_{p}^{2}/2m; \quad R_{\text{eff}}^{2} = R_{m}^{2} + T/(2\Delta_{p}^{2}T_{\text{eff}}).$$

Here T_{eff} and R_{eff} is effective temperature and radius of the emission region (source). Δ is the momentum spread dependent, in general, on type of collision, $\eta = 0.25$ is the fraction of the pions to be emitted from a static source (1-st generation particle) within unit of rapidity, R_m is the estimation of the source size (radius), $T \approx T_{ch}$ is the source temperature supposed equal to the parameter value at chemical freeze-out.

Parameterization for $\langle N_{ch} \rangle$ in $p+p$

The following functions are used for $p+p$ collisions:

a) hybrid function with aforementioned $\varepsilon \equiv s \,/\, s_0$, $s_0 = 1$ GeV^2

$$1.60 - 0.03 \ln \varepsilon + 0.18 \ln^2 \varepsilon + 0.03 \varepsilon^{0.29}; \qquad (1)$$

b) N^{3}LO pQCD function

$$\frac{K_{\mathrm{LHPD}}}{r_0} Y^{-a_1 c^2} \exp\left(2c\sqrt{Y} + \frac{c}{\sqrt{Y}} \left[r_1 + 2a_2 c^2 + \frac{\beta_1}{\beta_0^2} (\ln 2Y + 2) \right] \right.$$

$$\left. + \frac{c^2}{Y} \left[a_3 c^2 + \frac{r_1^2}{2} + r_2 - \frac{a_1 \beta_1}{\beta_0^2} (\ln 2Y + 1) \right] \right) + N_0, \qquad (2)$$

$$Y \equiv \ln(k_0 \sqrt{s} \,/\, 2\Lambda).$$

Parameterization for $\langle N_{ch}\rangle$ in A+A

Parameterizations for A+A collisions are two versions of the hybrid function

$$k(-0.577+0.394\ln\varepsilon+0.213\ln^{2}\varepsilon+0.005\varepsilon^{0.55}); \qquad (3)$$

$$k(0.512\varepsilon^{0.15}\ln\varepsilon+1.962), \qquad (4)$$

where $2k \equiv \langle N_{part}\rangle = (383 \pm 3)$ for central Pb+Pb collisions at $\sqrt{s_{NN}} = 2.76$ TeV.

p+*p*: density of charged particles

Fig. 23. Energy dependence of n_{ch} and critical parameter in p+p collisions. Solid line corresponds to the hybrid approximation (1) of N_{ch} and dashed line is for N^3LO pQCD equation (2).Critical density is shown by dotted line with its statistical uncertainty levels represented by thin dotted lines. The heavy grey lines correspond to the systematic ±1 s.d. of the quantity calculated by varying of η on ±0.05 [29].

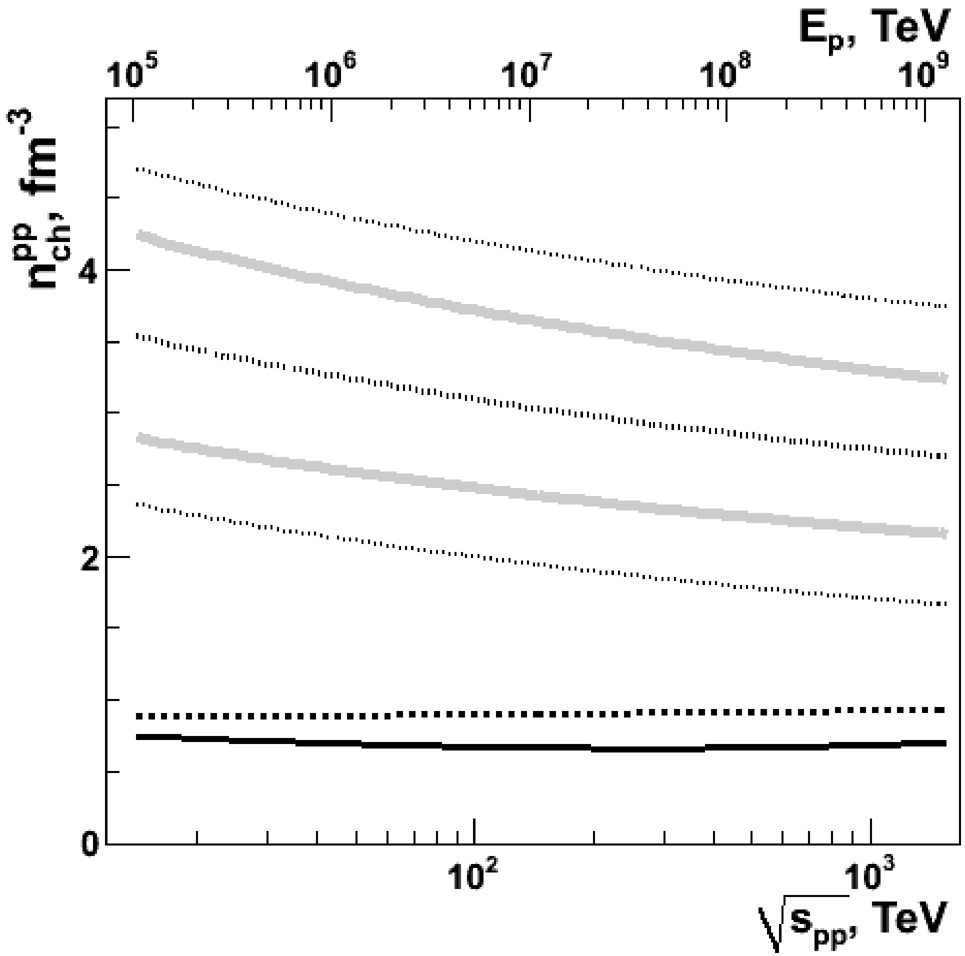

- The n_{ch} in $p+p$ is smaller than its critical value at collision energies up to $\sqrt{s_{pp}} \sim 1$ PeV.

A+A: density of charged particles

Fig. 24. Energy dependence of n_{ch} and critical parameter in symmetric (A+A) heavy ion collisions. Solid line corresponds to the hybrid approximation (3) of N_{ch} and dashed line is for equation (4). Critical density is shown by dotted line with its statistical uncertainty levels represented by thin dotted lines. The heavy grey lines correspond to the systematic ±1 s.d. of the quantity calculated by varying of η on ±0.05 [29].

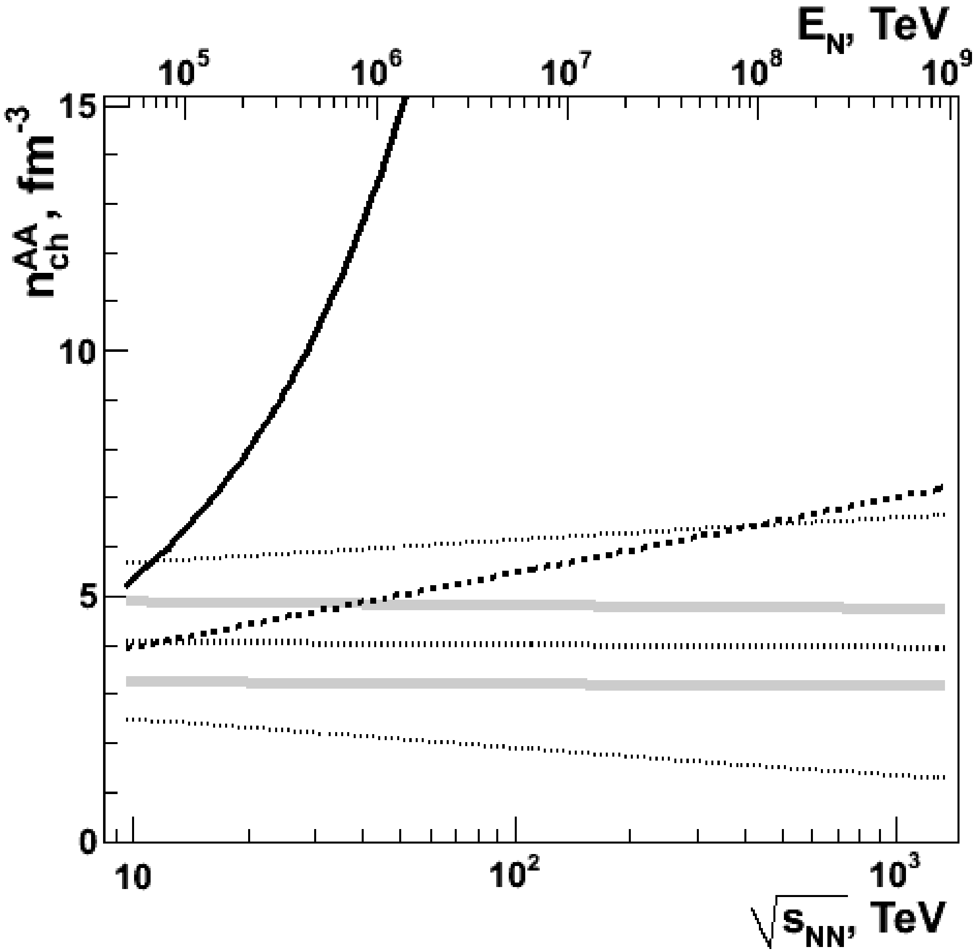

- The n_{ch} larger than its critical value at at any energies under consideration ($E_N \geq 10^{17}$ eV) for both equations (3) and (4) used for the approximation of $N_{ch}(\sqrt{s_{NN}})$.

BEC and multiplicity distribution

The influence of the Bose–Einstein condensation on secondary boson multiplicity was considered in [26] for the special case of the Poissonian multiplicity distribution.

The Poissonian distribution with mean n_0 is the following for the case when the Bose–Einstein effects are switched off

$$p_n^{(0)} = (n_0^n / n!) \exp(-n_0).$$

Then the probability distribution for the special case of the rare Bose gas, i.e. $X >> 1$, with taking into account the Bose–Einstein condensation, allows the analytic formula [26]

$$p_n = \frac{n_0^n}{n!} \exp(-n_0) \left[1 + \frac{n(n-1) - n_0^2}{2(4X)^{3/2}} \right]$$

with the mean value [26]

$$n = n_0 \left[1 + \frac{n_0}{(2X)^{3/2}} \right]. \qquad (5)$$

A+A: influence of BEC

Fig. 25. Energy dependence of n_{ch} *in symmetric (A+A) heavy ion collisions. The possible effect of the Bose–Einstein condensation is taken into account in accordance with (5) with* $X = 5$ *for the energy region with* $n_{ch} > n_c$*. Solid line correspond to the parameterization (3) for total multiplicity* N_{ch} *with thin line shown for the case of absence of BEC for completeness; dashed line is for the parameterization (4) [29].*

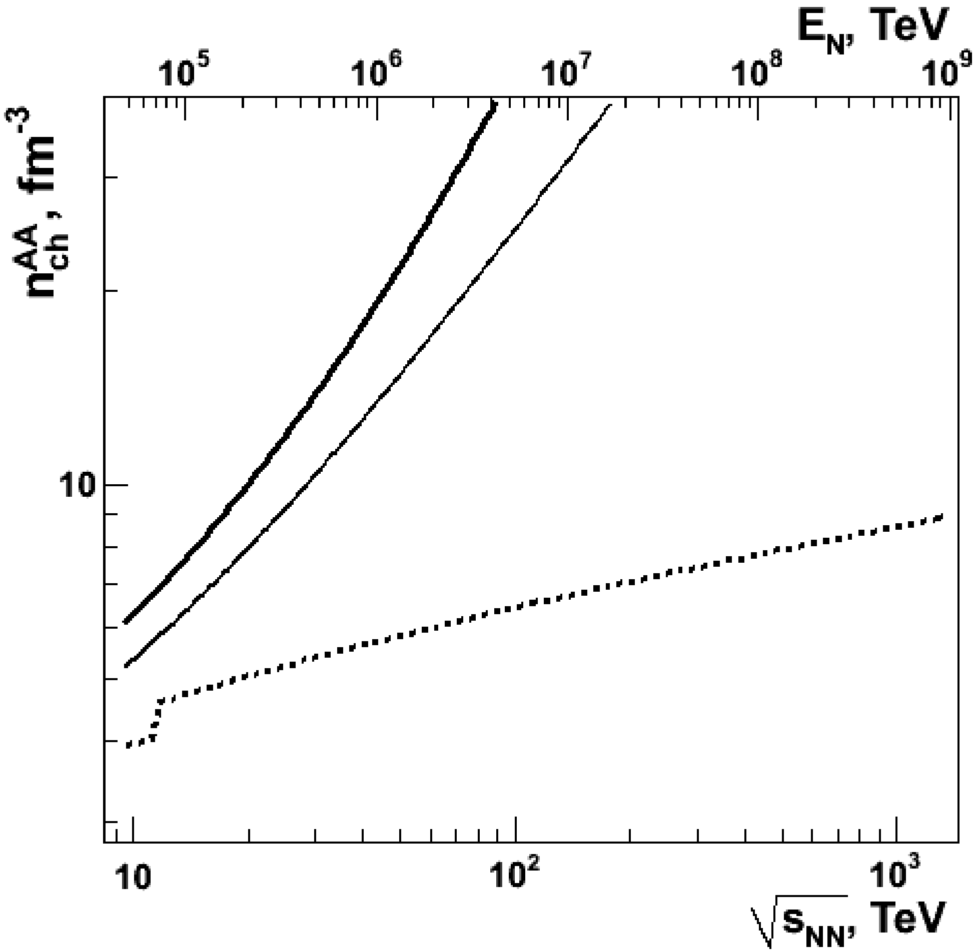

- The BEC results in to the visible increase of charged particle density at even large enough $X = 5$ for the energy range with $n_{ch} > n_c$.

Parameters for pion excess

The following characteristics have been determined in [29]

$$z_{\pi}^{(n)} = \frac{\ln n_{ch,\mathrm{BEC}}^{AA} - \ln n_{ch,0}^{pp}}{\ln n_{ch,0}^{AA} - \ln n_{ch,0}^{pp}},$$

$$\Delta z_{\pi}^{(n)} = z_{\pi}^{(n)} - 1.$$

Here $n_{ch,\,\mathrm{BEC}}$ is the density of charged particles (pions) with taking into account the possible Bose–Einstein condensation effect at the region with density larger than critical one ($n_{ch} > n_{c}$), $n_{ch,0}$ is the particle density when the Bose–Einstein effect is switched off.

The above parameters are used for quantitative study of the effect of Bose-Einstein condensation on the density of secondary charged pions and they are analogues of the corresponding quantities used in the study of muon excess in the collisions of UHECR particles.

Muon problem

Muon puzzle is a well-known problem in the physics of high-energy cosmic rays one of the aspects of which is the muon bundle excess compared to simulations within available phenomenological models [30, 31].

The dominant mechanism for the production of muons in air showers is via the decay of light charged mesons. Hadronic interaction models play a key role in our understanding of the physics driving the production of extended air showers (EASs) induced by UHECRs in the atmosphere.

Therefore the study of possible novel features in dynamics of multi-particle production processes allows the better understanding of the muon yield in UHECR particle collisions with atmosphere and can shed a new light on the muon problem.

BEC and muon production

A Poissonian emmiter that creates some number of bosons (pions), when symmetrization is ignored, would emit a very large number of bosons once symmetrization was included [24].

Due to decay mode

$$\pi^+ \to \mu^+ \nu_\mu, \quad \pi^- \to \mu^- \tilde{\nu}_\mu$$

with almost 99.99% fraction [8] the symmetrization effect for pions (BEC) could contribute to the enhancement for muon yield obtained in UHECR particle collisions.

A+A: z for n_{ch} with (3)

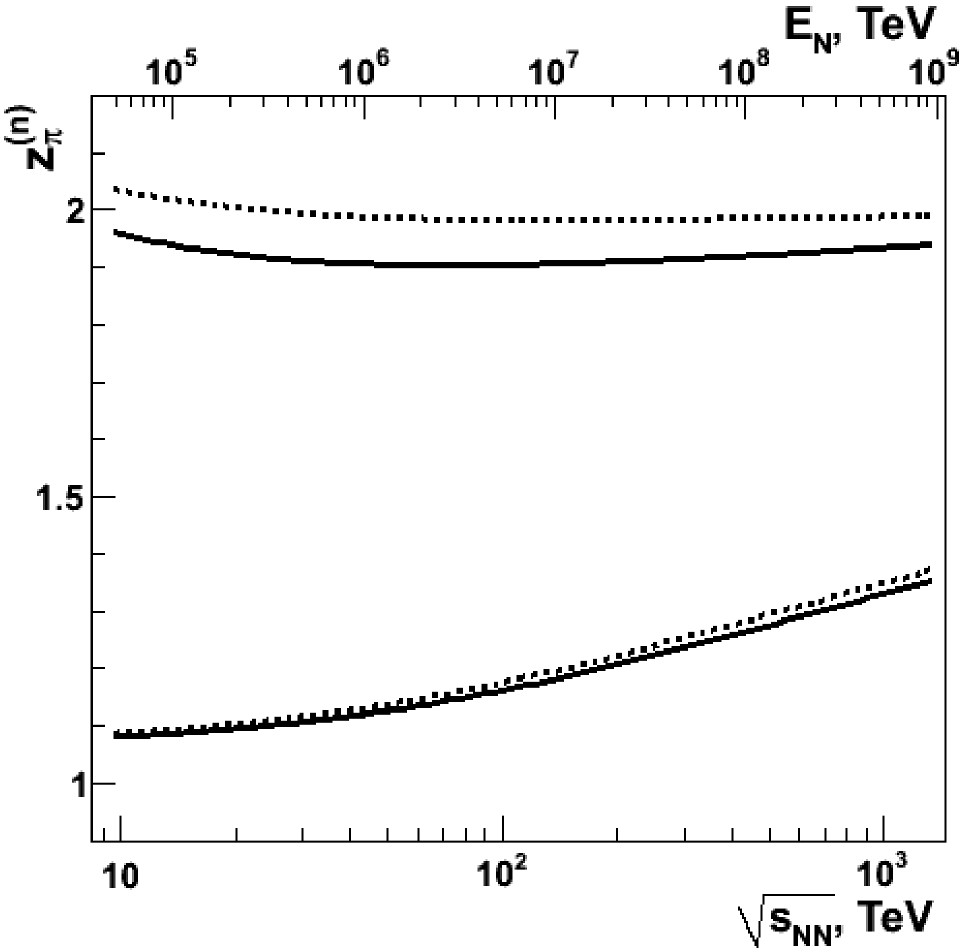

Fig. 26. Parameter z vs energy for n_{ch}. The parameterization (3) is used for total multiplicity N_{ch} for symmetric (A+A) heavy ion collisions. Solid lines correspond to the equation (1) for total multiplicity N_{ch} in p+p, dashed lines are for equation (2) for N_{ch} in p+p. Effect of BEC is taken into account in accordance with (5) for energy region with $n_{ch} > n_c$. The upper collection of curves corresponds to the X=0.5, lower curves are for X=5 [29].

- Curves $z(\sqrt{s_{NN}})$ show the close behavior for various parameterizations of N_{ch} in $p + p$, especially at larger X.

- The clear increase of z is observed with growth of energy at $X = 5$ whereas there is almost no dependence z vs $\sqrt{s_{NN}}$ at smaller X.

A+A: z for n_{ch} with (4)

Fig. 27. Parameter z vs energy for n_{ch}. The parameterization (4) is used for total multiplicity N_{ch} for symmetric (A+A) heavy ion collisions. Solid lines correspond to the equation (1) for total multiplicity N_{ch} in p+p, dashed lines are for equation (2) for N_{ch} in p+p. Effect of BEC is taken into account in accordance with (5) for energy region with $n_{ch} > n_c$. The upper collection of curves corresponds to the $X=0.5$, lower curves are for $X=5$ [29].

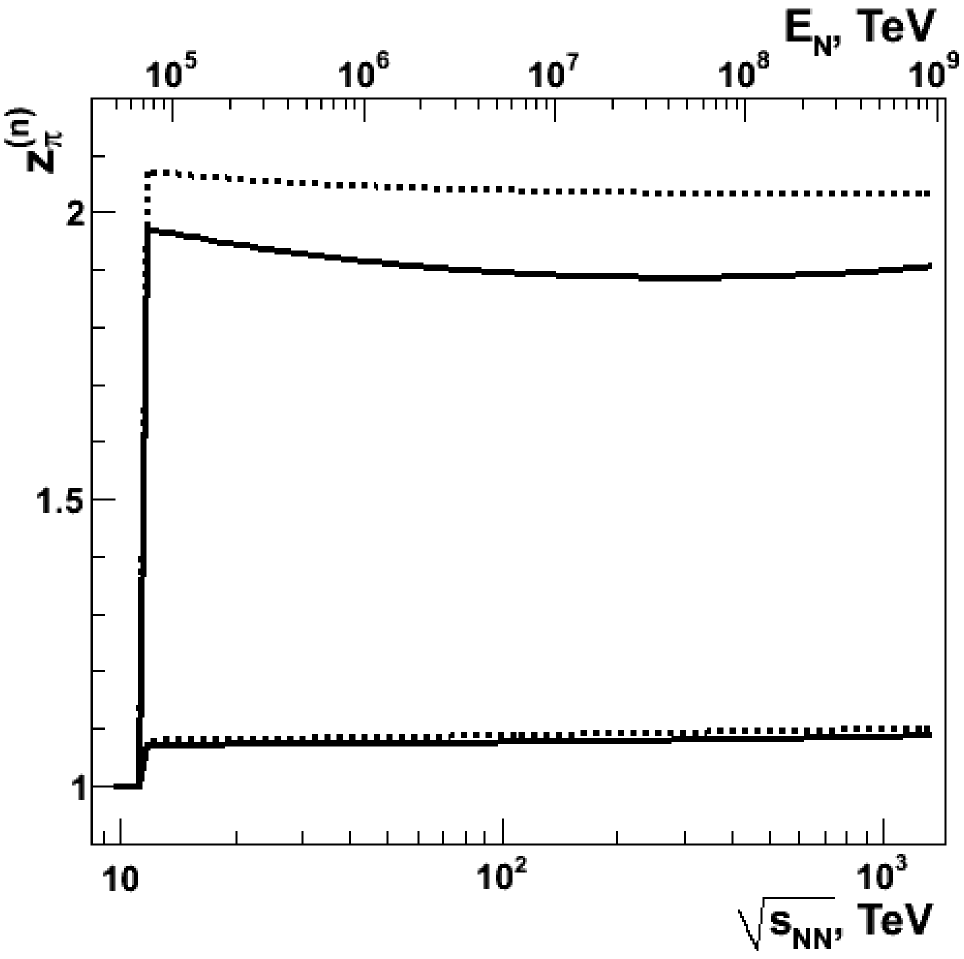

- Curves $z(\sqrt{s_{NN}})$ show the close behavior for various parameterizations of N_{ch} in $p+p$ at $X=5$ but values of z are noticeably larger for calculations with equation (2) than that for relation (1).

- The dependence z vs $\sqrt{s_{NN}}$ is significantly weaker for this case than that for the case of the equation (5) for total multiplicity N_{ch} in A+A collisions at both values of X used.

Summary (1)

In p+p collisions measurements for inclusive jet and dijet cross sections are extended to the multi-TeV region for kinematic parameters, namely, up to $p_T \approx 4$ TeV/c and $m_{jj} \approx 10$ TeV/c^2. Measurements of jet cross sections and strong coupling α_S are well agree with QCD calculations up to TeV energy scales.

At present it is rigorously established, in particular, with strong help of the study of collective effects, that collisions of subatomic particles in laboratory experiments produce hot matter consisting of deconfined quark and gluons – strongly coupled quark-gluon plasma (sQGP). Enormous efforts on theoretical and experimental studies of nuclear collisions during last decades resulted in to the "Standard model" of (heavy) ion collisions at high energies.

In nuclear collisions results for jets tagged by γ and heavy (c, b) quarks indicate that the energy loss depends on the color charge and possibly the mass of the parton. The cross sections are measured for top pair production in p+Pb and Pb+Pb collisions in multi-TeV energy domain. Studies of dijet momentum imbalance and event geometry confirm the path length dependence of energy loss of energetic partons inside hot quark-gluon matter.

Summary (2)

Femtoscopy provides direct experimental measurements for space-time extents of emission region as well as for hadron-hadron interactions including the case of presence of strongly interacting environment.

The correlations in particle pairs with low relative momentum are actively studied for very wide set of particle species. It should be noted that femtoscopic correlations are already measured for pairs including charmed mesons and light nucleus (d) in $p+p$ collisions at $\sqrt{s}$ = 13 TeV. The strangeness $|S| = 2$ and $|S| = 3$ sectors have been also recently studied using femtoscopic correlations Measured correlation functions demonstrate the attractive character of both p–Ξ and p–Ω interactions.

Significant overlap exists with the astrophysics community. The results obtained during recent years from femtoscopic measurements lead to more stringent constraints for single-parti-cle potentials and the EoS of dense baryonic matter. The EoS obtained with these constraints provides a stable NS with a maximum mass of $M = 2.13M_{\odot}$ and mass–radius dependence for NS which agree with astrophysical data.

Summary (3)

Collectivity opens a wide room for new mechanisms for multiparticle production at ultra-high collision energies.

Possibly, the Bose–Einstein condensation may affect on soft pion production in, at least, heavy nucleus collisions in multi-TeV range of $\sqrt{s_{\mathrm{NN}}}$. This phenomenon provides noticeable increase the mean values of particle density as well as total multiplicity of charged particles (pions). Future advancements in understanding the phase structure of strongly-interacting systems may come from considering similar or analogous observables in heavy-ion collisions and ultracold gases.

Aforementioned new feature of multiparticle processes can in the general case contribute to the muon yield recorded in collisions of UHECR particles with the atmosphere. Therefore, studying the possible BEC effect on the pion yield at ultra-high energies can be considered as one of perspective research directions for better understanding of the nature of the muon puzzle in UHECRs.

New stage for QCD

Due to modern facilities – RHIC and LHC – and large general-purpose detectors there is unique possibility for study of collectivity in multiparticle production processes driven by strong interaction with high precision in wide kinematic region.

The newly built sPHENIX detector and complementary upgrades of STAR detector at RHIC, together with increased luminosity at the LHC and upgraded detectors at ALICE, ATLAS, CMS and LHCb, will enable a multimessenger era for the physics of strong interaction, in particular, for QCD as the main candidate on the status of the theory of strong interaction.

References (1)

[1] J. Campbell, J. Huston, F. Krauss, *The black book of quantum chromodynamics*. Oxford: Oxford Univ. Press, 2018.
[2] M. Harrison, T. Lundlam, S. Ozaki, Nucl. Instr. Meth. A **499**, 235 (2003).
[3] *LHC design report*. Eds. O. Brüning et al., CERN-2004-003 **1** (2004).
[4] L. Evans, P. Bryant (eds.), J. Inst. **3**, S08001 (2008).
[5] *LHC design report*. Eds. M. Benedikt et al., CERN-2004-003 **3** (2004).
[6] K. Khelifa-Kerfa, arXiv: 2111.10671 [hep-ph].
[7] G. Aad et al. (ATLAS Collaboration), arXiv: 2404.06829 [hep-ex].
[8] R. L. Workman et al. (Particle data group), Prog. Theor. Exp. Phys. **2022** 083C01 (2022).
[9] A. Hayrapetyan et al. (CMS Collaboration), arXiv: 2405.16082 [hep-ex].
[10] S. Acharya et al. (ALICE Collaboration), Nature **605**, 440 (2022).
[11] S. Acharya et al. (ALICE Collaboration), arXiv: 2211.04384 [nucl-ex].
[12] *Proc. of the XXX International workshop on high energy physics*. Eds. V. Petrov, R. Ryutin. Singapore: World Scientific, 2015; p. 216.
[13] V. A. Okorokov, J. Phys. Conf. Ser. **1690**, 012006 (2020).
[14] V. A. Okorokov, Phys. At. Nucl. **86**, 742 (2022).
[15] G. Aad et al. (ATLAS Collaboration), arXiv: 2405.05078 [nucl-ex].
[16] A. M. Sirunyan et al. (CMS Collaboration), Phys. Rev. Lett. **125**, 222001 (2020).
[17] `https://alice.web.cern.ch/index.php/results`
[18] S. Acharya et al. (ALICE Collaboration), Phys. Lett. B **822**, 136708 (2021).
[19] L. Fabietti, V. Mantovani Sarti, O. Vázquez Doce, Annu. Rev. Nucl. Part. Sci **71**, 377 (2021).
[20] S. Acharya et al. (ALICE Collaboration), Phys. Rev. Lett. **123**, 112002 (2019).
[21] J. Adam et al. (STAR Collaboration), Phys. Lett. B **790**, 490 (2019).

References (2)

[22] `https://en.wikipedia.org/wiki/Bose-Einstein_condensate`
[23] G. Jannes, PhD thesis. Madrid, 2009.
[24] S. Pratt, Phys. Lett. B **301**, 159 (1993).
[25] T. Csörgő, J. Zimányi, Phys. Rev. Lett. **80**, 916 (1998).
[26] J. Zimányi, T. Csörgő, Heavy Ion Phys. **9**, 241 (1999).
[27] V. A. Okorokov, Adv. High Energy Phys. **2016**, 5972709 (2016).
[28] V. A. Okorokov, Phys. At. Nucl. **82**, 838 (2019).
[29] V. A. Okorokov, Phys. At. Nucl. **87**, 172 (2024).
[30] A.A. Petrukhin, Nucl. Instr. Meth. Phys. Res. A **742**, 228 (2014).
[31] H.P. Dembinski et al., Eur. Phys. J. Web Conf. **210**, 02004 (2019).

Thanks for you attention